A new RC bond model suitable for three-dimensional cyclic analyses

Luís A. M. Mendes[a,b,], Luís M. S. S. Castro[a,c]

[a]Instituto de Engenharia de Estruturas, Território e Construção, Av. Rovisco Pais 1, 1049-001 Lisboa, Portugal
[b]Laboratório Nacional de Engenharia Civil, Av. do Brasil 101, 1700-066 Lisboa, Portugal
[c]Instituto Superior Técnico, Universidade Técnica de Lisboa, Av. Rovisco Pais 1, 1049-001 Lisboa, Portugal

---

Abstract

This paper introduces an original model to simulate the bond failure between concrete and reinforcing steel bars. The model was developed to be used in three-dimensional analyses within the framework of the Finite Element Method and for general loading cases. It was designed using a hierarchical approach by combining what is called the *base model*, which acts as the skeleton of the model and introduces the basic response under monotonic and reversed loading, and four independent and optional sub-models used to enhance the simulation when needed, by considering the cyclic resistance degradation, the peak stress slip evolution, the reload slip evolution and the radial stress effect.

The model implementation within the framework of the Finite Element Method is described and its accuracy is assessed using a series of validation tests. At the end, the main conclusions extracted from this work are presented.

Keywords: Concrete-Steel Bond, Reinforced Concrete, Inelastic Behaviour, Cyclic Analysis

---

Email address: `luismendes77@gmail.com` (Luís A. M. Mendes)

Preprint submitted to Computers and Structures *January 28, 2013*

1. INTRODUCTION

For economic reasons, common *reinforced concrete* (RC) structures are designed in such way that they dissipate energy with large inelastic deformations when subjected to severe earthquakes or other intense load sources. In those situations, RC elements are exposed to high loading demands that can lead to a strong nonlinear response.

A particular vulnerable component is the connection between the reinforcing bars and the concrete that in the scope of this paper will be called the *concrete-steel interfaces* (CSI). These interfaces play the important role of transmitting forces between the reinforcements and the concrete and incorporate the well-known and complex longitudinal stress transfer mechanism, commonly called the *bond mechanism*, but also the radial stress transfer that develops at these interfaces.

When the forces to be transmitted are too high, the perfect connection between both materials is lost and relative displacements occur. This can influence the amount, size and distribution of cracks, potentiate higher stiffness and resistance degradation, intense stress redistributions and result in significant changes in the response. In particular, the hysteretic response may be characterized by long branches with reduced stiffness and pinching effects, which contributes decisively to narrower cycles, and consequently, to lower hysteric energy dissipation.

2. PROBLEM FORMULATION

2.1. Modelling scale

The first issue to be taken into consideration is what scale should be used to represent the bond mechanism. This is a fundamental aspect since all subsequent modelling options will be influenced by this choice. The classification adopted by Lowes [1] seems to be appropriate and may be summarized as follows.

Modelling the bond mechanism at the *element scale* using a global response constitutive relation has the advantage of being extremely effective from the computational point of view, because all the inelastic response, including bond and other inelastic sources, is included in a single force *vs.* displacement or moment *vs.* curvature relation. The main drawbacks are related to not considering the inelastic response distributed along the element and the reduced adaptability to other geometries and reinforcement configurations.

Adopting the *rib scale* representation of the bond mechanism all bond-related elements are geometrically incorporated in the model, including the ribs of the reinforcements and the concrete keys between them. This methodology has the advantage of being extremely general and potentially very accurate. However, it is necessary to adopt complex constitutive models and the resulting problem-size is generally only practical for local simulations, *e.g.* for model calibration.

A possible compromise solution would be to model the concrete-steel bond at the *reinforcement scale*. This approach uses a single constitutive relation, commonly defined in terms of bond stress *vs.* slip, to simulate all inelastic phenomena associated with the combined response of the reinforcement surface and of the surrounding concrete (*e.g.* concrete cracking and crushing). This constitutive relation usually requires the definition of interface elements that include the reinforcement surface and the surrounding concrete. The combination of the bond response into a single model will mean that different bond characteristics (*e.g.* different rib types, different levels of corrosion or different concrete casting conditions) will require different bond constitutive relations. This approach is considered to be the most feasible and it is adopted in the bond model proposed in this paper.

2.2. Main quantities involved

Let us consider the small domain of the RC element represented in Figure 1-a. This domain includes the reinforcing bar, with diameter ϕ_s, and the surrounding concrete. For the sake of simplicity, this domain will be considered as two-dimensional without compromising the generality of the formulation that can always be expanded to the general three-dimensional case, in a straightforward manner. This domain has been subjected to a set of loads that induced relative displacements between the reinforcement and the concrete, as shown in Figure 1-b. The relative displacements along the axis of the reinforcement bar $q_1^{rel}(x_1)$ are commonly called *slips* $s(x_1)$ and the relative displacements perpendicular to the axis of the bar $q_2^{rel}(x_1)$ are addressed in this paper by *radial relative displacements* $r_2(x_1)$ or simply by *opening/closing displacements*.

According to Figure 1, for each point along the axis of the reinforcement bar, these relative displacements can be defined as follows:

$$q_1^{rel}\left(x_1\right) = s\left(x_1\right) = q_1^A - q_1^B = q_1^A - q_1^C, \tag{1}$$

$$q_2^{rel}\left(x_1\right) = r_2\left(x_1\right) = \left(q_2^B - q_2^A\right) - \left(q_2^C - q_2^A\right) = q_2^B - q_2^C. \tag{2}$$

The adoption of equations (1) and (2) implies the following sign convention: positive slips correspond to protruding reinforcements in the edge with higher x_1 coordinate and positive radial displacements implies opening movements.

As represented in Figure 1-c, associated with the slips and radial displacements are the bond stress τ_b and the radial stress σ_{r2}. The equivalent global forces for the domain represented in Figure 1 can be computed from:

$$Q_s = \int_0^L \tau_b P_c, dx_1, \tag{3}$$

$$Q_{r2} = \int_0^L \sigma_{r2}, dx_1, \tag{4}$$

where P_c is the *contact perimeter* by unit length defined by the perimeter of a circle with diameter ϕ_s, and thus, neglecting the contribution of the ribs. These expressions imply that τ_b and σ_{r2} only vary along x_1 and that the bond stress is defined by perimeter unit, contrary to the radial stress.

3. MECHANICAL CHARACTERIZATION OF THE BOND MECHANISM

Most of the authors producing work in this field agree that the bond between steel and concrete results from the combined effect of chemical adhesion between cement paste and steel, friction between surfaces and mechanical resistance associated with the ribs. As a consequence, for ribbed bars, the bond strength results from the combined strength of all these three effects, generally much higher than the strength for smooth bars, where only adhesion and friction contributes to the resistance. Furthermore, the mechanical resistance associated with the ribs includes the shear resistance of the concrete between ribs and the resistance associated with the compression struts generated by splitting forces (see Figure 2).

A recurrent way of studying the bond mechanism is by the analysis of experimental results. The failure mode in basic bond tests, e.g. pull-out tests, is likely to be triggered by splitting or cylindrical cracks, or by concrete cone failure or reinforcing steel yield. If the last two failure modes are avoided, the bond stress *vs.* slip relation for monotonic loading (see Figure 2) is mainly influenced by the existence of ribs and by the confinement level.

For what concerns the response under cyclic or alternated loading, the bond performance presents additional stiffness and strength degradation caused by progressive micro-cracking and concrete crushing. According to FIB [2], the most important factors influencing this degradation are the *type of ribs* and the *slip history*, which can be quantified by the *maximum slip* reached in both directions s_{max}.

Apart from these quantities, other aspects influencing the bond mechanism are the geometric characteristics of the ribs, the steel bar diameter, the concrete characteristics, the level of radial stress, the loading rate, the existence of steel bar corrosion, the occurrence of yielding and the bond-related size effect. More information on these subjects can be found in the following references [1, 2, 3, 4].

4. DEVELOPMENT OF THE BOND MODEL

4.1. Introduction

This section is devoted to the development of a new bond model designated *Concrete-Steel Interface* (CSI) model. The model is designed to be used in large three-dimensional simulations that require all constituent parts to be as efficient as possible. Consequently, considering the analysis presented in section 2, it is possible to conclude that the most feasible approach is to develop a semi-analytical model implemented at the reinforcement scale.

The subsequent step is to define the phenomena to be incorporated in the model, always by balancing the quality of the simulation against the additional complexity and computational cost to be paid. At first, the model must simulate the main phenomena experienced under monotonic loading. In addition, it is designed to be used under general loading situations, such as earthquake loading. Therefore, it is mandatory that the model is prepared for dealing with reversed cyclic loading, meaning that the cyclic degradation and other response characteristics must be included. Some effects, like the loading rate and the steel bar corrosion cannot be explicitly simulated by the proposed model. Nevertheless, these can be simulated to some extent by adjusting the model parameters.

It was considered preferable to have a simpler model formulation, even if sometimes the local accuracy would be compromised, than a complex mathematical definition. This option is supported by the assumption that for real situations the global response of a reinforced concrete structural element is much more influenced by spatial bond failure variations than by complex local model definitions. As a result, linear branches were most of the times used to connect the key points used to define the model.

Finally, the formulation of the proposed bond model will be developed in several phases to separate as much as possible each feature and to develop a hierarchical-based solution. The starting point is what is called the *base model* that will act as the skeleton and includes the most important response characteristics. Afterwards, this base is enriched with optional sub-models with the purpose of simulating specific bond-related phenomena.

4.2. Base model

Figure 3 presents a schematic plot of the base model under monotonic and reversed cyclic loading. This model is characterized by:

1. Under monotonic loading (see Figure 3-a), the response starts with a stiffer linear loading branch with slope k_{pb}, until the slip value s_{pb} is reached. Afterwards, another linear loading branch connects the point at coordinates $(s_{pb}, \tau_{pb} = k_{pb} s_{pb})$ to the peak stress at $(s_0, \tau_0 = k_0 s_0)$. The peak stress is followed by a softening branch to $(s_{res}, \tau_{res}^{ld} = f_1 \tau_0)$ and by a loading sliding friction plateau at stress level τ_{res}^{ld};

2. Under cyclic loading (see Figure 3-b), to cope with the stiff unloading branches observed in the experimental programs, a k_{ul} slope is adopted for the unloading branches. Under reversed loading, an unloading sliding friction stress is reached at stress level $\tau_{res}^{uld} = f_2 \tau_0$, after the bond stress changes sign. Reloading occurs in order to connect the friction stress at null slip to the peak stress τ_0 again at s_0. It should be noted that the stiffer loading branches with slope k_{pb} only occur for the first complete loading cycle.

Figure 4 compares the results obtained by this model with the average monotonic and cyclic responses reported by Eligehausen *et al.* [3]. It can be easily observed that the monotonic response can be very well simulated with the base model. On the other hand, under reversed loading, there is a clear difference between the experimental and numerical results. The main differences are related to the incorrect peak stress simulation after the first loading, the incorrect simulation of the slip where reloading occurs and the incorrect simulation of the peak stress slip also after the first loading. In order to overcome these difficulties, the base model is enriched with a series of sub-models that are described in the following subsections.

The shape of the softening branch can be defined as nonlinear by changing the value of the parameter c_s defined afterwards in section 5. This parameter can be set to zero resulting in a linear branch, or to values greater than zero that will result in increasing smother transitions to the residual loading plateau. Figure 5 illustrates the effect of this parameter in the numerical simulations previously presented in Figure 4.

4.3. Sub-model for the cyclic resistance degradation

The experimental data represented in Figure 6 was obtained by Eligehausen *et al.* [3] by performing a series of pull-out tests under reversed loading with reinforced concrete specimens constructed with common reinforcing bars and concrete. The data presents the ratio between the stress before unloading at cycle n and the one for the first cycle. This quantity gives information related to the cyclic resistance degradation and is considered to be strongly related to the cyclic peak stress ratio defined by:

$$\gamma_b(n) = \frac{\tau_0^n}{\tau_0^1}. \tag{5}$$

Two distinct factors are presented together in Figure 6, namely the cycle amplitude and the number of cycles. These two factors can be combined into an equivalent value by introducing the non-negative parameter:

$$s^* = \frac{1}{s_0} \sum_{n=1}^{ncyc} \tilde{s}_k, \tag{6}$$

where $ncyc$ represents the number of cycles and $\tilde{s}_k$ represents the absolute value of the loading slip reached in each cycle and the sum is normalized by the initial peak stress slip. As an example, in the cases presented in Figure 6 the cycles have equal amplitude, so the following expression may be used to compute s^*:

$$s^* = (2n + 1)\, \frac{s_{max}}{s_0}. \tag{7}$$

The same data represented in Figure 6 is re-plotted in Figure 7, showing a clear trend and correlation with the proposed parameter s^* and relatively small data dispersion.

The following expression is used to approximate the cyclic peak stress ratio using the parameter s^*:

$$\gamma_b(s^*) = a \exp(-bs^*) + c \exp(-ds^*) + e. \tag{8}$$

The unknown coefficients can be computed by a nonlinear fit using the *Levenberg-Marquardt* algorithm [5, 6] resulting in $a = 0.5838$; $b = 0.0792$; $c = 0.3456$; $d = 3.8290$ and $e = 0.0887$. The resulting curve is also presented in Figure 7 and it is possible to observe the good quality of the data fit.

The adopted exponential relation (8) returns $\gamma_b(0) \approx 1.0$ and converges asymptotically to the value at $\gamma_b(\infty)$. For $s^* = 100$ it returns values already very close ($< 0.24\%$) to the value for very large values of s^*. Thus, this function is truncated at $s^* = 100$ for simplicity.

Although the expression presented in equation (8) is closely related to this specific experimental data, it can be redesigned to be more general and adaptable to other situations. With that purpose, two new parameters were inserted: i) γ_{res} that represents the residual cyclic resistance ratio after an infinite number of cycles and ii) γ_n that can be used to change the shape of the curve and gives more flexibility and generality to the sub-model. The enhanced expression is given by:

$$\gamma_b(s^*) = \frac{\gamma_{res}}{1-e}\left\{a \exp(-b\gamma_n s^*) + c \exp(-d\gamma_n s^*)\right\} + \gamma_{res}. \tag{9}$$

Changing the values of parameter γ_{res} modifies the final value of the cyclic peak stress ratio without changing the shape of the curve (see Figure 8-a). On the contrary, changing γ_n has the opposite effect (see Figure 8-b).

The implementation of this sub-model into the bond model can be done simply by scaling the peak stress value, previously defined by $\tau_0 = k_0 s_0$, using the factor $\{1 - \gamma_b(s^*)\}$, where s^* is defined for the previous completed semi-cyclic using equation (6):

$$\tau_0^*(s^*) = \{1 - \gamma_b(s^*)\}\,\tau_0. \tag{10}$$

Consequently, the loading and unloading residual stress plateaus, which are related to the peak stress, are now defined respectively by $f_1\tau_0^*$ and $f_2\tau_0^*$. Figure 8-c presents a schematic representation of this sub-model implementation.

The same analysis case considered to compute the data represented in Figure 4-b can be re-used to compute the data represented in Figure 8-d, considering now the cyclic resistance degradation. Comparing both figures, it is possible to conclude that this enhancement in the bond model has a large impact in the quality of the simulation.

4.4. Sub-model for the peak stress slip evolution

The data collected in experimental results shows that the slip value in which the peak stress is reached is not constant for all the phases characterizing the bond mechanism. In fact, this data shows an increasing tendency that can be related to the fact that a higher relative displacement is necessary to mobilize all available strength after concrete cracking and crushing.

This is clearly visible in the results obtained by Eligehausen *et al.* [3], as shown in Figure 4-b. This behaviour is considered an important aspect of the bond mechanism. Hence, to improve the quality of the simulation, a sub-model will be added to the base model to simulate this effect. The following assumptions for the slip in which the peak stress is reached were adopted:

1. this value increases with the development of inelastic phenomena at the interface;
2. this value varies between s_0 that characterizes the response for the virgin state and the value for the beginning sliding friction plateau s_{res}.

The following expression is adopted for the sub-model:

$$s_{pk}\left(s^*\right) = s_0 + \left(s_{res} - s_0\right)\left(\frac{s^*}{100}\right)^{n_{pk}}, \tag{11}$$

where s_{pk} is the slip value in which the peak stress is reached; n_{pk} is a non-negative parameter used to change the profile of the evolution as showed in Figure 9-a, and s^* is the parameter used before.

Figure 9-b presents a schematic representation of the effect of this sub-model in the simulation.

4.5. *Sub-model for the reload slip evolution*

For the reloading branches, the experimental results also show that the slip in which the stiffness increases changes throughout the tests. This can also be clearly observed in the results obtained by Eligehausen *et al.* [3] presented in Figure 4-b. For this factor, a clear pattern cannot be observed for the evolution. It seems indubitable that this slip value has the tendency to move into the loading sliding friction plateau. However, the starting and ending slip values, and also, the evolution pattern are not clearly recognizable from the available data. Consequently, the sub-model must be more flexible in order to adapt to different situations.

The following expression is adopted to simulate the reload slip evolution:

$$s_{rld}\left(s^*\right) = s^0_{rld} + \left(s^\infty_{rld} - s^0_{rld}\right)\left(\frac{s^*}{100}\right)^{n_{rld}} \leq s^\infty_{rld}, \tag{12}$$

where s_{rld} represents the slip value in which the reloading branch begins; s^* is the parameter used in the previous sub-models; s^0_{rld} represents the initial value at $s^* = 0$; s^∞_{rld} corresponds to the final value at $s^* = 100$, and as before, n_{rld} allows changing the shape of the evolution as represented in Figure 10-a.

Note that the signs of both s^0_{rld} and s^∞_{rld} are not associated with the absolute slip values. Instead, they correspond to a relative slip in which the negative values are associated with the anticipation of the reload branch, and thus, positive values mean delaying the reload branch. It should be taken into consideration that if the cycle amplitude is not enough to exceed s^0_{rld}, the reload offset must be truncated to this value. Figure 10-b presents a qualitative representation of the sub-model effect in the simulation.

Figure 11 presents a comparison with the experimental data considered previously. It is possible to observe that adding the sub-models for the simulation of the cyclic resistance degradation, of the evolution of peak stress slip and of the reload slip has significantly improved the simulation quality.

4.6. Sub-model for the radial stress effect

To introduce the radial stress effect into the bond model, it is necessary to have information about the stress in the surrounding concrete. A difficulty emerges because the concrete stress is not reflected in the interface element that is used within the framework of the Finite Element Method. A possible solution is to enhance the state determination of the interface element with information from other elements. This will be performed by adopting a procedure similar to the one used for the nonlocal regularization technique to cope with localization problems [7, 8].

The first step is to compute the perpendicular direction to the interface axis in the direction towards the reference Gauss point. This can be performed by the following procedure.

Let us consider the two Gauss points drawn in black in Figure 12. The Gauss point labelled GP_{ref} belongs to the interface element and the one labelled GP_k is part of the surrounding concrete. It is possible to define the unit vector $\mathbf{v}_1$ with the direction connecting the position of these points, using their global coordinates $\mathbf{X}$:

$$\mathbf{v}_1 = \frac{\mathbf{X}^{GP_k} - \mathbf{X}^{GP_{ref}}}{\left\|\mathbf{X}^{GP_k} - \mathbf{X}^{GP_{ref}}\right\|}. \tag{13}$$

Another unit vector can be defined with the direction of the central axis of the interface element. Considering that a zero-thickness interface element with linear geometry is used in the implementation, this direction can be computed using the expression:

$$\mathbf{v}_2 = \frac{\mathbf{X}^{II} - \mathbf{X}^{I}}{\left\|\mathbf{X}^{II} - \mathbf{X}^{I}\right\|}, \tag{14}$$

where $\mathbf{X}^k$ is the global coordinate of the local node k.

Note that $\mathbf{v}_1$ and $\mathbf{v}_2$ are not necessarily perpendicular to each other. To correct this, the following equation can be applied:

$$\mathbf{v}_3 = \mathbf{v}_2 \times \mathbf{v}_1, \tag{15}$$

and finally, the unit vector $\mathbf{n}$ that is perpendicular to $\mathbf{v}_2$ and points towards GP_k is given by:

$$\mathbf{n} = \mathbf{v}_3 \times \mathbf{v}_2. \tag{16}$$

The radial stress is the component of the stress vector acting in the direction defined by $\mathbf{n}$ and it can be computed using:

$$\sigma_{rad} = \sigma_{ij} n_i n_j. \tag{17}$$

A weighted average value for the radial stress σ_{rad} is used to improve the quality and representativeness of the stress value in the surrounding concrete, by computing:

$$\bar{\sigma}_{rad} = \sum_{k=1}^{nGP} (\sigma_{rad}\ W)_k, \tag{18}$$

where W is the weight associated with each Gauss point (GP) selected.

The selection of the eligible Gauss points and the computation of the weights can be made using a similar approach to the one used in nonlocal constitutive relations [7, 8] by using the *Gaussian function* or the *bell-shaped function* [9]. A new parameter called the *bond length* L_b is introduced to characterize the width in which the bond mechanism develops. This way, the weights of each Gauss point can be computed from:

$$W_{gp} = \frac{1}{W_{tot}} f\left(L_b, \mathbf{X}^{GP_{ref}}, \mathbf{X}^{GP_k}\right), \tag{19}$$

where $\mathbf{X}^{GP_{ref}}$ and $\mathbf{X}^{GP_k}$ are the coordinates of the reference and of the selected Gauss points. To enforce that the sum of the weights is unitary, the parameter W_{tot} is computed from:

$$W_{tot} = \sum_{k=1}^{nGP} W_k. \tag{20}$$

The final step consists in defining the sub-model for the radial stress effect. This is done using the parameter η, which effect is represented in Figure 13 and defined by:

$$\eta\left(\bar{\sigma}_{rad}\right) = \begin{cases} \eta_0 + (\eta_- - \eta_0)\left(\frac{|\bar{\sigma}_{rad}|}{f_c}\right)^{n_{\eta-}} \leq \eta_-, & \text{if } \sigma_{rad} < 0 \\ \eta_0 & \text{if } \sigma_{rad} = 0, \\ \eta_0 + (\eta_+ - \eta_0)\left(\frac{|\bar{\sigma}_{rad}|}{0.10 f_c}\right)^{n_{\eta+}} \geq 0, & \text{if } \sigma_{rad} > 0 \end{cases} \tag{21}$$

where η_0 is the value of the function in the absence of radial stress, η_- and η_+ are the values for $\bar{\sigma}_{rad} = -f_c$ and for $\bar{\sigma}_{rad} = 0.1 f_c$, respectively, and $n_{\eta-}$ and $n_{\eta+}$ are exponents used to define the shape of the function for negative and positive values of the radial stress. The reference value of $0.1 f_c$ was adopted to avoid the explicit definition of another parameter.

One possible way to introduce this effect into the bond model is to scale the reference slips s_{pb} and s_0, using the following expressions:

$$s_{pb}(\eta) = s_{pb}(\eta_0)\,\eta, \tag{22}$$

$$s_0(\eta) = s_0(\eta_0)\,\eta. \tag{23}$$

This would result in the desired uniform change of the peak stresses and of the corresponding slip values. However, it does not change the slopes of most branches, even when the radial stress changes throughout the analysis, as exemplified in Figure 14-a for constant radial stress. Furthermore, the beginning slip for the residual friction stress level s_{res} is considered to be unchanged by the radial stress. These assumptions are supported by observations made on experimental results [3, 10, 11, 12]. Figure 14-b presents an example of the constitutive relation with constant and without the radial stress effect for reversed cyclic loading.

5. MATHEMATICAL FORMULATION

5.1. State determination algorithm

The bond model is defined by the parameters presented in Table 1 and the constitutive relation adopts the following expression:

$$\tau_b = k_{ul}\,(s - s_{ine})\,, \tag{24}$$

where k_{ul} is the unloading stiffness and s_{ine} is the inelastic slip.

A *bond envelope function* $\phi_b^{\pm}$ is defined for the positive and for the negative limit of the bond stress. Taking advantage of the fact that these are odd functions, it is possible to write a condensed expression that can be used for either the positive and negative envelops[1]:

---

[1] The symbol ± should be replaced by a + or a − sign, resulting in the positive and negative limit of the envelope function

$$\phi_b^{\pm} = \begin{cases} \pm\alpha, & \text{if } \pm s \leq s_{rld} \\ \pm f_2 \tau_0^* \eta_{pk} \pm \frac{\tau_0^* \eta_{pk}(1-f_2)}{s_{pk}\eta_{pk}-s_{rld}} \left(\pm s - s_{rld}\right), & \text{if } s_{rld} < \pm s \leq s_{pk} \\ \pm\beta \pm \lambda \left\{\tau_0^* \left(\eta_{pk} - f_1 \tau_0^*\right) + \frac{\tau_0^*\left(f_1 \eta - \eta_{pk}\right)}{s_{res}-s_{pk}\eta_{pk}} \left(\pm s - s_{pk}\eta_{pk}\right)\right\}, & \text{if } s_{pk} < \pm s \leq s_{res} \\ \pm\beta, & \text{if } s_{res} < \pm s \end{cases}, \tag{25}$$

with:

$$\alpha = f_2 \tau_0^* \eta; \quad \beta = f_1 \tau_0^* \eta; \quad \tau_0^* = (1-\gamma_b)\, k_0 s_0; \quad \lambda = \exp\left(-c_s \frac{\pm s - s_{pk}\eta_{pk}}{s_{res} - s_{pk}\eta_{pk}}\right). \tag{26}$$

During the first load, the envelope function is changed to:

$$\phi_b^{\pm} = \begin{cases} k_{pb} s, & \text{if } |s| \leq s_{pb}\eta_{pk} \\ \pm k_{pb} s_{pb} \eta_{pk} + \frac{k_0 s_0 - k_{pb} s_{pb}}{s_{pk}-s_{pb}} \left(s - s_{pb}\eta_{pk}\right), & \text{if } s_{pb}\eta_{pk} < |s| \leq s_{pk} \end{cases}. \tag{27}$$

The symbol η_{pk} refers to the value of parameter η defined in equation (21) when the peak stress is reached. This value is used to define the slope of the softening branch, so it must be stored until the end of each loading cycle.

The admissible values for the bond stress are limited by the positive and negative envelope functions:

$$\phi_b^- \leq \tau_b \leq \phi_b^+. \tag{28}$$

This condition must be satisfied in the state determination procedure. With that purpose, the following procedure may be adopted: i) Compute the trial bond stress τ_b^{trial} for the current slip value using the expression (24); ii) If τ_b^{trial} violates the limits imposed by equation (28) then correct the inelastic slip s_{ine} using:

$$s_{ine} = s - \phi_b^{\pm}/k_{ul}, \tag{29}$$

where in this case $\phi_b^{\pm}$ should be replaced by the violated envelope function.

5.2. Stiffness matrix

The total derivative of the bond stress must be computed in order to obtain the tangential components of the interface element stiffness matrix. As seen before, the bond stress is a function of the slip and a set of state parameters that only changes between cycles, with the exception of radial stress that can change without any constraint. Therefore, the total derivative can be expressed as:

$$d\tau_b = \frac{\partial \tau_b}{\partial s} ds + \frac{\partial \tau_b}{\partial \eta} d\eta. \tag{30}$$

It is not possible to compute the term $\partial\tau_b/\partial\eta$ within the element scope, as parameter η depends on $\bar{\sigma}_{rad}$, which is defined by the averaged information from the surrounding concrete elements.

To mitigate this problem, the model was developed in such way that the slope of branches #1, #2 and #6 represented in Figure 15 are not affected by the changes of $\bar{\sigma}_{rad}$. In these cases, quadratic convergence may be achieved even if the radial stress changes. On the other hand, for the other branches the quadratic convergence is lost. Nonetheless, even in those situations the convergence reveals to be quite efficient and fast, as a consequence of the changes of slope being relatively small.

The term $\partial\tau_b/\partial s$ in equation (30) can be computed for each branch represented in Figure 15, from:

$$\partial\tau_b/\partial s = \begin{cases} k_{pb}, & \text{case \#1} \\ \frac{k_0 s_0 - k_{pb} s_{pb}}{s_{pk} - s_{pb}}, & \text{case \#2} \\ \frac{\tau_0^*(f_2-1)\eta_{pk}}{s_{pk}\eta_{pk} - s_{rld}}, & \text{case \#3} \\ \frac{\tau_0^*\left(f_1\eta - \eta_{pk}\right)}{s_{res} - s_{pk}\eta_{pk}}, & \text{case \#4 (if } c_s = 0) \\ 0, & \text{case \#5} \\ k_{ul}, & \text{case \#6} \\ 0, & \text{case \#7} \end{cases} . \tag{31}$$

For case #4, when $c_s > 0$, the derivative turns into:

$$\frac{\partial\tau_b}{\partial s} = \frac{c_s\left\{\tau_0^*\left(f_1\eta - \eta_{pk}\right) - \frac{\tau_0^*\left(s - \eta_{pk}s_{pk}\right)\left(f_1\eta - \eta_{pk}\right)}{s_{res} - s_{pk}\eta_{pk}}\right\}}{\exp\left\{\frac{c_s\left(s - s_{pk}\eta_{pk}\right)}{s_{res} - s_{pk}\eta_{pk}}\right\}\left(s_{res} - s_{pk}\eta_{pk}\right)} + \frac{\tau_0^*\left(f_1\eta - \eta_{pk}\right)}{\exp\left\{\frac{c_s\left(s - s_{pk}\eta_{pk}\right)}{s_{res} - s_{pk}\eta_{pk}}\right\}\left(s_{res} - s_{pk}\eta_{pk}\right)}. \tag{32}$$

6. MODEL IMPLEMENTATION

A discontinuity in the displacement field is created when the bond between reinforcement and concrete starts to fail. This discontinuity corresponds to relative displacements between adjacent points in the domain. In the scope of the Finite Element Method, these displacement discontinuities can be simulated in several ways. It is possible to classify them as: i) *element-based*, when the discontinuity is embedded inside the element and no mesh modification is required; and ii) *mesh-based*, when the discontinuity simulation requires the addition of nodes and/or special interface elements. This latter approach is adopted in this work.

Although the so-called *hanging nodes* were not adopted in this work, they can introduce some advantages into the simulation, in particular for the concrete mesh generation, resulting in a reduction of degrees of freedom. Using this approach the reinforcement nodes are not required to be coincident with the concrete element nodes, as they can be located on their edges/faces, and the concrete displacements may be computed from finite element interpolations. This technique has been addressed by several authors [13, 14, 15] and intense research is being made in the integration with the *eXtended Finite Element Method* (X-FEM) [16], *e.g.* [17, 18, 19].

For what concerns the meshing technique, interface elements in parallel with the main domain are adopted. This technique presents some advantages related to the fact that the mesh is simpler to be generated even for three-dimensional analyses because the concrete sub-domain is unaffected and continuous. Its main disadvantage is that the interface element is insensitive to the stress state on the concrete domain.

The type of interface element to be implemented is another option that needs to be taken. Zero-thickness elements are adopted in this work due to its formulation and implementation simplicity and to the fact that accurate results can be obtained. These elements were originally developed by Goodman *et al.* [20] and enhanced by Beer [21] and Carol and Alonso [22] that presented an isoparametric zero-thickness element to be used for interfaces. The element works as one-dimensional due to the consideration of the mechanical formulation in the interface mid-plane.

Another option would be to adopt thin-layer elements [23, 24, 25, 26]. These elements consider that the interface mechanism occurs in a narrow finite zone and models the interfaces as thin continuum elements. This technique was not adopted because setting the correct thickness for each problem with an objective procedure is sometimes not easy to accomplish and numerical problems have been reported for some types of these elements with very small thickness, *e.g.* degenerated standard continuum elements [4].

6.1. Interface element

The interface element combines the CSI model described in the previous sections and additional elastic models for the radial directions, which are defined using large numerical values for the stiffness. The objective is to impose near null radial relative displacements between the steel and concrete elements adopting a procedure similar to a penalty method.

The isoparametric zero-thickness interface element proposed by Beer [21] is adopted. The element kinematics includes the longitudinal relative displacement (slips) and the radial relative displacements (opening and closure movements). These kinematic variables can be joined together in the following vector:

$$\mathbf{q}^{rel} = \left[\begin{array}{ccc} s & r_2 & r_3 \end{array} \right]^t, \tag{33}$$

where s devotes the slip between concrete and reinforcement and r_i corresponds to the radial relative displacement (opening/closure) along the local direction i.

The associated static variables can be grouped in the following stress vector:

$$\boldsymbol{\sigma} = \left[\begin{array}{ccc} \tau_b & \sigma_{r2} & \sigma_{r3} \end{array} \right]^t, \tag{34}$$

where τ_b represents the tangential stress (bond stress) created by the slips and σ_{ri} are the radial stresses associated with the radial displacement along the local direction i.

The following expressions are adopted for the element mapping [21]:

$$x_k^{bot} = \psi_1 y_k^{[I]} + \psi_2 y_k^{[II]}, \tag{35}$$

$$x_k^{top} = \psi_2 y_k^{[III]} + \psi_1 y_k^{[IV]}, \tag{36}$$

and for the relative displacement approximations [21]:

$$q_k^{bot} = \psi_1\, q_k^{[I]} + \psi_2\, q_k^{[II]}, \tag{37}$$

$$q_k^{top} = \psi_2\, q_k^{[III]} + \psi_1\, q_k^{[IV]}, \tag{38}$$

where the shape functions ψ_k are defined as first order polynomials (see Figure 16).

The relative displacement approximations can be computed from the top and bottom edge displacements (see Figure 16), using [21]:

$$q_k^{rel} = q_k^{top} - q_k^{bot} = \psi_2 q_k^{[III]} + \psi_1 q_k^{[IV]} - \psi_1 q_k^{[I]} - \psi_2 q_k^{[II]}. \tag{39}$$

Note that for dynamic analyses the velocity and acceleration approximations can be computed from similar expressions to those presented for the displacements in equations (37), (38) and (39).

This formulation results in a model that directly relates the stresses with the relative displacements. Hence, the compatibility equations are not similar to the ones used in the continuum mechanics framework, which involves derivatives. Instead, they are simply defined by differences between displacements.

The compatibility relations can be computed from:

$$\mathbf{q}^{rel} = \mathbf{B}\,\mathbf{q}, \tag{40}$$

with:

$$\mathbf{B} = \left[\begin{array}{ccc|ccc|ccc|ccc} -\psi_1 & 0 & 0 & -\psi_2 & 0 & 0 & \psi_2 & 0 & 0 & \psi_1 & 0 & 0 \\ 0 & -\psi_1 & 0 & 0 & -\psi_2 & 0 & 0 & \psi_2 & 0 & 0 & \psi_1 & 0 \\ 0 & 0 & -\psi_1 & 0 & 0 & -\psi_2 & 0 & 0 & \psi_2 & 0 & 0 & \psi_1 \end{array}\right]. \tag{41}$$

The following constitutive relation is considered for the interface element:

$$\boldsymbol{\sigma} = \mathbf{k}^{*} \left(\mathbf{q}^{rel} - \mathbf{q}^{rel}_{ine} \right), \tag{42}$$

where $\mathbf{k}^{*}$ is the *inelastic constitutive tensor* and $\mathbf{q}^{rel}_{ine}$ corresponds to the *inelastic displacement vector*, non-null only for the slip component:

$$\mathbf{k}^{*} = \begin{bmatrix} k^{*}_{s} & 0 & 0 \\ 0 & k_{r2} & 0 \\ 0 & 0 & k_{r3} \end{bmatrix}, \tag{43}$$

$$\mathbf{q}^{rel}_{ine} = \begin{bmatrix} s_{ine} & 0 & 0 \end{bmatrix}^{t}, \tag{44}$$

where k^{*}_{s} represents the *secant modulus* defined by $k^{*}_{s} = \tau_{b}/s$.

The stiffness matrix can be obtained from [27]:

$$\mathbf{K} = \int_{-1}^{1} \mathbf{B}^{t}\left(y_{1}\right)\ \mathbf{k}^{*}\, \mathbf{B}\left(y_{1}\right)\ \det \mathbf{J}\left(y_{1}\right) \mathrm{d}y_{1}, \tag{45}$$

and the *secant stiffness matrix* can be computed using the Gauss-Legendre quadrature:

$$\mathbf{K}_{s} = \sum_{gp=1}^{ngp} \mathbf{B}^{t}\left(y_{1}\right)_{gp} \mathbf{k}^{*}_{gp} \mathbf{B}\left(y_{1}\right)_{gp} \det \mathbf{J}\left(y_{1}\right)_{gp} w_{gp}. \tag{46}$$

where $\mathbf{J}$ is the Jacobian matrix and w is the quadrature weight associated with each Gauss point. In this work, two Gauss points were used to compute the previous expression.

The use of the *tangent stiffness matrix* can enhance the computational efficiency of the numerical model by increasing the convergence rate. This matrix can be computed using [28]:

$$\mathbf{K}_t = \frac{\partial \mathbf{Q}_i}{\partial \mathbf{q}} = \int \mathbf{B}^t \frac{\partial \boldsymbol{\sigma}}{\partial \mathbf{q}} d\Omega, \tag{47}$$

where $\mathbf{Q}_i$ represents the *internal force vector*.

Considering the relation (40), the stress derivative term can be computed from:

$$\frac{\partial \boldsymbol{\sigma}}{\partial \mathbf{q}} = \frac{\partial \boldsymbol{\sigma}}{\partial \mathbf{q}^{rel}} \frac{\partial \mathbf{q}^{rel}}{\partial \mathbf{q}} = \frac{\partial \boldsymbol{\sigma}}{\partial \mathbf{q}^{rel}} \mathbf{B}, \tag{48}$$

where for the radial components the $\partial \boldsymbol{\sigma} / \partial \mathbf{q}^{rel}$ term corresponds to the radial stiffness k_{ri} along each radial direction i as in equation (43). On the other hand, the bond-related component is given by $\partial \tau_b / \partial s$, defined in Section 5.

As before, the stiffness matrix can be computed using the Gauss-Legendre quadrature:

$$\mathbf{K}_t^{el} = \sum_{gp=1}^{ngp} \mathbf{B}^t (y_1)_{gp} \left(\frac{\partial \boldsymbol{\sigma}}{\partial \mathbf{q}^{rel}} \right)_{gp} \mathbf{B} (y_1)_{gp} \det \mathbf{J} (y_1)_{gp} \, w_{gp}, \tag{49}$$

with:

$$\frac{\partial \boldsymbol{\sigma}}{\partial \mathbf{q}^{rel}} = \begin{bmatrix} \frac{\partial \tau_b}{\partial s} P_c & 0 & 0 \\ 0 & k_{r2} & 0 \\ 0 & 0 & k_{r3} \end{bmatrix}, \tag{50}$$

where P_c is the contact perimeter described in Section 2.

7. EXAMPLE 1 - PULL-OUT TESTS BY ELIGEHAUSEN, BERTERO AND POPOV

The objective of this example is to simulate the response of the pull-out tests performed by Eligehausen *et al.* [3]. These tests were considered as an ideal case for a first validation, because there is an extensive amount of data available and a short anchorage was used ($5d_b = 127$ mm), which creates a nearly uniform response throughout the anchorage.

Figure 17 presents the main geometric and mechanical characteristics of the tests. A plane model was used to simulate the experiment and the concrete was modelled with isoparametric 4-noded elements (Q4), adopting an elastic constitutive relation. The steel bar was simulated with elastic Euler-Bernoulli beam (EBB) elements, although one-dimensional truss elements could also have been used, similar to what was done in Example 2. The interface elements are modelled using the proposed CSI element. All the parameters required by the models are presented in Table 2.

This series of tests was executed by prescribing a set of quasi-static displacements and measuring the equivalent force on one side of the protruding steel reinforcement bar (point A on Figure 17) and by measuring the displacement on the other side of the bar (point B). A set of boundary conditions were enforced at the concrete nodes near point A, as presented in Figure 17.

Three static analyses were performed (see Table 3). In the first analysis a monotonic displacement is imposed and no active confinement (radial stress) is taken into account. The second test simulates the reversed cyclic response of the interface, again with no imposed radial stress. This effect is studied in detail in the third analysis by considering four levels of radial stress.

7.1. Case 1 - Monotonic loading with no radial stress

Figure 18 presents the results of the analysis #1 expressed in a diagram relating the constraint force at point A (Q_C) and the displacement measured at point B (q_B). These values are compared with the average value of the group of monotonic tests carried out by Eligehausen *et al.* [3] expressed in terms of bond stress *vs.* slip. As one will see further on, the structural response reveals that the behaviour of the interface is not uniform. However, the variations are minimum, and consequently, it can be assumed that a good approximation can be obtained from $\tau_b \approx Q_c/A_c$, where A_c is the *contact area* given by the *contact perimeter* P_c multiplied by the *contact length* L_c. This relation considers that the force associated with the prescribed displacement can be transformed into the equivalent bond stress assuming a uniform stress throughout the anchorage length. The bond stresses obtained through this relation will be represented by τ_b^{eq} and denoted by the *equivalent bond stress* to avoid confusions. Figure 18 was drawn using two vertical axes that were scaled using this formula to enable a direct comparison. For simplicity, this hypothesis will be adopted throughout this example.

The results presented in Figure 18 show a very good match between the experimental response obtained by Eligehausen *et al.* [3] and the numeric data obtained with the numerical model. The model was capable of reproducing all the phases of the monotonic response, namely: i) the initial stiffer loading branch; ii) the stiffness decrease until peak stress is reached; iii) the peak stress value; iv) the softening branch and v) the sliding friction residual stress.

Figures 19, 20 and 21 present a series of numerical results obtained at the Gauss points of the interface elements at peak force ($q_{imp} = -1.975$ mm, step #79).

Figure 19 represents the slip variation and these results confirm that this variable is not uniform along the anchorage. As expected, the slips are larger near the loaded edge and smaller at the other end. This figure also shows the plot of the bond stress along the interface, revealing that the stress distribution is also not uniform, although the variations are relatively small. It can be seen that the interface zone for $x \geq 200$ mm is still loading and that the zone closer to the loading end, with smaller x values, is already in the softening branch. The *equivalent bond stress* (τ_b^{eq}) that is obtained by assuming a uniform slip distribution is also presented in this figure using a dotted line. It is possible to conclude that this approximation is feasible and can be used for the analysis of the results with a minor loss of accuracy.

Figure 20 presents the axial stress distribution along the reinforcement bar. As expected, it can be seen that the stress is approximately uniform along the first and last third of the bar length, as the reinforcing steel bar is not connected to the concrete by interface elements in those regions (see Figure 17). Inside the specimen, the stress gradually reduces to zero due to the loading and boundary conditions.

The concrete stress σ_{xx} distribution is also plotted in Figure 20 for the Gauss points closer to the interface. The results show compression stresses near the loading edge, tensile stresses near the free edge and a transition zone in the middle of the specimen. This observation is confirmed by the concrete principal stress vectors at peak force represented in Figure 21. Furthermore, it is visible that along the bond length, the transition from a predominant compression to tensile states is accompanied by a rotation of the principal stress directions creating radial stresses (see Figure 21).

7.2. Case 2 - Reversed cyclic loading with no radial stress

This analysis has the objective of testing the model in the simulation of pull-out tests with reversed loading. The model parameters are listed in Table 2 and are identical to the ones adopted for the monotonic loading case, with the inclusion of calibrated parameters for simulating the cyclic resistance degradation, the peak stress slip evolution and the reload slip evolution. The parameters related to the radial stress effect were left neutral, *i.e.* with no effect on the simulation. The loading history for this analysis is indicated in Table 3.

The equivalent bond stress *vs.* slip diagram is presented in Figure 22 and is plotted against the experimental data obtained by Eligehausen *et al.* [3]. It is possible to observe a good match between both curves and conclude that the experimental response was simulated with a good level of accuracy.

7.3. Case 3 - Monotonic loading with variable levels of radial stress

The objective of this analysis is to assess the capacity of the proposed numerical model to simulate the effect of active radial stresses.

The starting point of this analysis is to calibrate the sub-model for the radial stress effect defined in Section 4 with the pre-existing data from the tests. This was done by fitting this data using the *Levenberg-Marquardt* algorithm [5, 6], in order to find the best values for the parameters η_- and $n_{\eta-}$ associated with compressive radial stresses. The resulting sub-model curve is presented in Figure 23-a and reveals a very good match with the experimental data, showing that the sub-model is flexible enough to reproduce this data. In addition, no information is available for characterizing the effect of tensile radial stresses so that no data fit was made for the sub-model parameters associated with the tensile domain, which were left neutral, *i.e.* with no effect on the simulation ($\eta_+ = 1.0, n_{\eta+} = 1.0$). This effect is only relevant for the case where no radial stress is applied to the specimen, because radial tensile stresses can occur in the interface. In all other cases, the compression stresses are enough to eliminate this possibility.

For this simple two-dimensional analysis case it is possible to present a schematic representation of how the nonlocal radial stress is computed. In Figure 23-b it can be seen that for each interface Gauss point, a group of concrete Gauss points are chosen using a criterion related to the adopted *bond length* L_b. The *bell-shaped function* is used to compute the weights of the Gauss points [9] and these values are represented in Figure 23-b by the shade level of each Gauss point, using blacker shades for larger weights and lighter shades for smaller weights.

A series of analyses were performed for the four levels of imposed radial stress $\sigma_{rad} = \{0.0, -5.0, -10.0, -13.2\}$ MPa, which were applied in the first loading step and kept constant throughout the analysis. The equivalent bond stress *vs.* slip diagrams are presented in Figure 24. The results show a very good match between the numerical and experimental results, not only in terms of the calibrated peak stress, but also in terms of the shape of the loading, softening and sliding friction plateau.

In addition, Figure 25 presents the computed nonlocal radial stresses along the interface elements at the steps associated with branch switching points on Figure 24-c. As mentioned before, the pull-out forces generate additional compression and tension stresses at the interface (see Figure 19), so as expected, the radial stress distribution is not uniform along the anchorage length. Moreover, higher radial stress variations occur when the pull-out force is larger (peak stress at $q_{imp} = -2.375$ mm).

8. EXAMPLE 2 - PULL-OUT TESTS BY LA BORDERIE AND PIJAUDIER-CABOT

The pull-out tests performed by La Borderie and Pijaudier-Cabot [10] are used to validate the model in a three-dimensional analysis case. The geometric and mechanical characteristics of this experimental programme, together with the mesh and boundary conditions adopted are summarized in Figure 26. The anchorage length is 45 mm, approximately $5.6\phi_s$, which can be classified as a small anchorage. Hence, it is expected that the strain and stress fields will be nearly uniform. Table 4 lists the details of all models used. The concrete was modelled using elastic (model #1) three-dimensional isoparametric 8-noded hexahedral elements (H8), the reinforcements were modelled with one-dimensional elastic (model #2) truss elements (L2) and the concrete-steel interface is simulated using the proposed CSI model (model #3).

Four analyses were performed by changing the radial stress in both horizontal directions to $\sigma_{rad} = \{0.0, -5.0, -10.0, -15.0\}$ MPa. The load was imposed as a monotonic quasi-static displacement at the protruding steel bar. As before, the parameters for simulating the radial stress effect were computed by fitting the experimental data, using the *Levenberg-Marquardt* algorithm [5, 6], by finding the best values for the parameters η_- and $n_{\eta-}$ for the compression domain of the radial stress equation, leading to $\eta_0 = 1.000$, $\eta_- = 1.293$ and $n_{\eta-} = 0.347$.

For the analysis with no radial stress, Figure 27-a presents a graphical representation created from the σ_{zz} values at the concrete Gauss points. This figure shows the expected stress distribution, with stress concentrations near the extremity of the bar embedded in the concrete and near the protruding bar zone.

The tensile stress concentration inside the specimen could result in cracking and the elastic model used to simulate the concrete response was not able to capture this effect. Nevertheless, this effect is only local and would not significantly influence the pull-out test results. Furthermore, the axial stress distribution along the reinforcing bar is presented in Figure 27-b. These results confirm the gradual stress transfer between the steel bar and the concrete.

In Figure 28, the applied force *vs.* the prescribed displacement at point A is plotted for the four tested cases of radial stress, together with the experimental data obtained by La Borderie and Pijaudier-Cabot [10]. From the analysis of this figure it is possible to observe a good match between the experimental and numerical results. In particular, setting the parameter c_s to values greater than zero made possible to follow with greater accuracy the softening branch of the bond mechanism. Moreover, it is possible to conclude that, after being calibrated, the model was able to accurately simulate the behaviour observed in all the tests.

Figure 29 presents the axial stress along the steel reinforcing bar for the analysis without radial stress. The stress distribution in the steel reinforcement reveals a smooth transmission of forces into the concrete, confirming what was observed in Figure 27-b.

9. CONCLUSIONS

This paper introduces an original bond model to simulate the mechanical interaction between concrete and reinforcing steel bars, when loaded beyond the perfect bond limit. The model is deemed to be used in three-dimensional analyses within the framework of the Finite Element Method and for general loading cases.

The so-called CSI model makes possible to include an extensive list of phenomena affecting bond mechanism, which led to 22 model parameters. This number is considered high and a drawback of the proposed model. To mitigate this problem, the bond model was developed using a hierarchical approach, by defining a base model with 9 parameters and a group of 4 sub-models for the simulation of the cyclic degradation, the peak stress slip evolution, the reload slip evolution and the radial stress effect, using 2, 1, 3 and 7 additional parameters, respectively. This hierarchical approach makes possible the use of the model for reversed loading cases by defining only the 9 parameters required for the base model and by setting the other parameters to default values. Each sub-model can be added only if the simulated phenomenon is significant for the response. As an overall assessment, it is possible to stress that the proposed solution presents a balanced and robust way to simulate the large majority of the phenomena that characterize the bond mechanism.

The use of zero-thickness interface elements to simulate bond failure within three-dimensional finite element meshes revealed to be a feasible and reasonable procedure.

Taking into consideration the results from the validation examples presented in this paper, it is possible to conclude that the proposed bond model is able to simulate with a very good accuracy level the bond response observed in pull-out tests, both for monotonic and cyclic loading.

At this stage, it would be very interesting to continue the model validation with other test results, in particular, with long anchorages specimens and with data from dynamic bond tests. Furthermore, taking advantage of hanging nodes to simplify the concrete mesh generation is another improvement scheduled for future work.

10. ACKNOWLEDGEMENTS

The authors would like to acknowledge and emphasize the importance of the financial support given to this research by *Fundação para a Ciência e a Tecnologia* through the doctoral grant with reference SFRH/BD/21491/2005/J03122797V2. In addition, all the support gave by Laboratório Nacional de Engenharia Civil (LNEC), in particular by Dr. Ema Coelho, is greatly recognized and appreciated.

References

[1] L. N. Lowes, Finite element modeling of reinforced concrete beam-column bridge connections, Ph.D. thesis, University of California (1999).

[2] FIB, Bond of reinforcement in concrete, Tech. rep., International Federation for Structural Concrete (FIB) (2000).

[3] R. Eligehausen, V. Bertero, E. Popov, Local bond stress-slip relationships of deformed bars under generalized excitations, Tech. rep., Earthquake Engineering Research Center, University of California (1983).

[4] N. Dominguez, Etude de la liaison acier-béton: De la modélisation du

phénoméne à la formulation d'un elément fini enrichi "béton armé", Ph.D. thesis, L'Ecole Normale Supérieure de Cachan (2005).

[5] K. Levenberg, A method for the solution of certain problems in least squares, Quarterly of Applied Mathematics 2 (1944) 164–168.

[6] D. Marquardt, An algorithm for least-squares estimation of nonlinear parameters, SIAM Journal on Applied Mathematics 11 (1963) 431–441.

[7] Z. Bažant, T. Belytschko, T. Chang, Continuum model for strain softening, Journal of Engineering Mechanics (ASCE) 110 (1984) 1666–1692.

[8] G. Pijaudier-Cabot, Z. Bažant, Nonlocal damage theory, Journal of Engineering Mechanics 113 (10) (1987) 1512–1533.

[9] M. Jirásek, Objective modeling of strain localization, Revue Française de Génie Civil 6 (6) (2002) 1119–1132.

[10] C. La Borderie, G. Pijaudier-Cabot, Etude expérimentale du comportement des matériaux renforcés, Tech. rep., LMT Cachan (1987).

[11] L. J. Malvar, Bond of reinforcement under controlled confinement, Tech. rep., Naval Civil Engineering Laboratory (1991).

[12] L. J. Malvar, Bond of reinforcement under controlled confinement, ACI Materials Journal 89 (6) (1992) 593–601.

[13] A. K. Gupta, A finite element for transition from a fine to a coarse grid, International Journal for Numerical Methods in Engineering 12 (1) (1978) 35–45.

[14] M. Ainsworth, B. Senior, Aspects of an adaptive hp-finite element method: Adaptive strategy, conforming approximation and efficient solvers, Computer Methods in Applied Mechanics and Engineering 150 (1-4) (1997) 65–87.

[15] M. Donglin, S. McFee, Irregular triangles for finite element analysis in electromagnetics, Magnetics, IEEE Transactions on 35 (3) (1999) 1422–1425.

[16] I. Babuska, J. Melenk, The partition of unity method, International Journal for Numerical Methods in Engineering 40 (4) (1997) 727–758.

[17] M. Ainsworth, L. Demkowicz, C.-W. Kim, Analysis of the equilibrated residual method for a posteriori error estimation on meshes with hanging nodes, Computer Methods in Applied Mechanics and Engineering 196 (37-40) (2007) 3493–3507.

[18] P. Šolín, J. Cervenỳ, I. Doležel, Arbitrary-level hanging nodes and automatic adaptivity in the hp-fem, Mathematics and Computers in Simulation 77 (1) (2008) 117–132.

[19] T.-P. Fries, A. Byfut, A. Alizada, K. W. Cheng, A. Schröder, Hanging nodes and xfem, International Journal for Numerical Methods in Engineering 86 (4-5) (2011) 404–430.

[20] R. E. Goodman, R. L. Taylor, T. L. Brekke, A model for the mechanics of jointed rock, Journal of the Soil Mechanics and Foundations Division ASCE 94 (SM3) (1968) 637–659.

[21] G. Beer, An isoparametric joint/interface element for finite element analysis, International Journal for Numerical Methods in Engineering 21 (4) (1985) 585–600.

[22] I. Carol, E. E. Alonso, A new joint element for the analysis of fractured rock, in: 5th Int. Congr. Rock Mech., Vol. Vol. F, Melbourne, Australia, 1983, pp. 147–151.

[23] C. S. Desai, M. M. Zaman, J. G. Lightner, H. J. Siriwardane, Thin-layer element for interfaces and joints, International Journal for Numerical and Analytical Methods in Geomechanics 8 (1) (1984) 19–43.

[24] O. C. Zienkiewicz, B. Best, C. Dullage, K. Stagg, Analysis of nonlinear problems in rock mechanics with particular reference to jointed rock systems, in: 2nd International Congress on Rock Mechanics, Belgrade, 1970.

[25] J. Ghaboussi, E. Wilson, J. Isenberg, Finite element for rock joints and interfaces, Journal of the Soil Mechanics and Foundations Division, ASCE, 99 (SM10) (1973) 833–48.

[26] K. G. Sharma, C. S. Desai, Analysis and implementation of thin-layer element for interfaces and joints, Journal of Engineering Mechanics 118 (12) (1992) 2442–2462.

[27] K. J. Bathe, Finite Element Procedures, Prentice-Hall, New Jersey, 1996.

[28] M. A. Crisfield, Non-Linear Finite Element Analysis of Solids and Structures - Volume 1: Essentials, John Wiley & Sons Ltd, New York, 1991.

List of Figures

1 Denomination of the basic CSI quantities 38
2 Typical response under monotonic loading, adapted from FIB [2]. 39
3 Schematic representation of the base model. 40
4 Base model - Comparison with experimental data. 41
5 Effect of the parameter c_s in the simulation. 42
6 Bond strength deterioration with the number and amplitude of the cycles, adapted from Eligehausen *et al.* [3]. 43
7 Relation between the cyclic peak stress ratio and the parameter s^*. 44
8 Sub-model for the cyclic resistance degradation. 45
9 Sub-model for the peak stress slip evolution. 46
10 Sub-model for the reload slip evolution. 47
11 Comparison of the results obtained with the proposed bond model with experimental data. 48
12 Radial stress effect - Computing the stress acting on the interface. 49
13 Radial stress effect: Influence of the parameters on the shape of the function η. 50
14 Radial stress effect for reversed cyclic loading. 51
15 Bond model branch numbering. 52
16 Zero thickness 4-noded isoparametric interface element. 53
17 Example 1 - Geometric and mechanical characteristics and mesh used in the analyses. 54
18 Example 1 (#1) - Response under monotonic loading 55
19 Example 1 (#1) - Bond stress and slip variation along the interface at peak force. 56
20 Example 1 (#1) - Steel axial stress and surrounding concrete stress at peak force. 57
21 Example 1 (#1) - Principal stress vectors in the concrete elements at peak force. 58
22 Example 1 (#2) - Equivalent bond stress *vs.* slip. 59
23 Example 1 (#3) - Radial stress sub-model. 60
24 Example 1 (#3) - The effect of the radial stress. 61
25 Example 1 (#3) - Computed nonlocal radial stresses along the anchorage ($\sigma_{rad} = -10.0$ MPa). 62
26 Example 2 - Geometric and mechanical characteristics and mesh used in the analyses. 63
27 Example 2 - Analysis without external radial stress ($\sigma_{rad} = 0.0$ MPa, $q_{imp} = 1.20$ mm). 64
28 Example 2 - The effect of the radial stress on the monotonic response. 65

29 Axial stress distribution along the interface at chosen steps (σ_{rad} = 0.0 MPa). 66

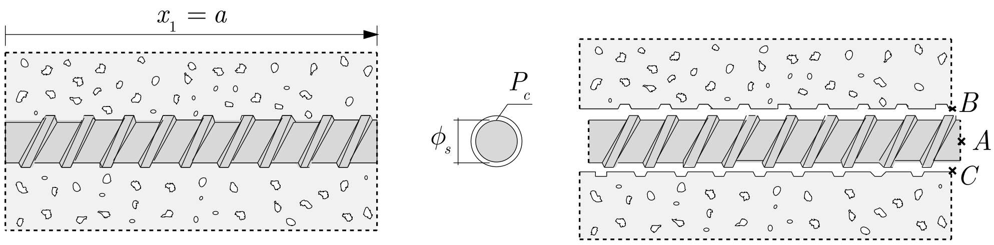

(a) undeformed

(b) deformed

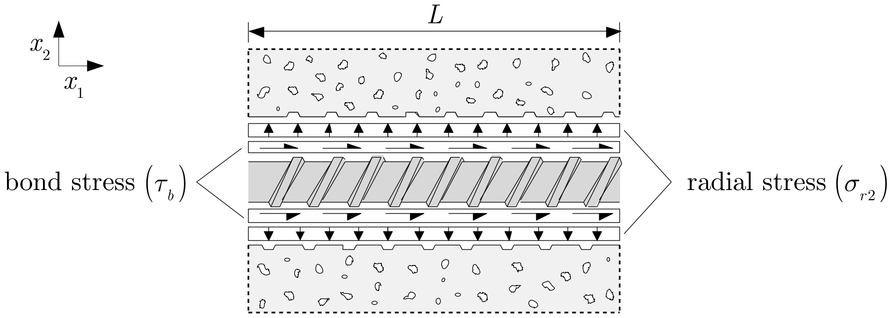

(c) stresses

Figure 1: Denomination of the basic CSI quantities

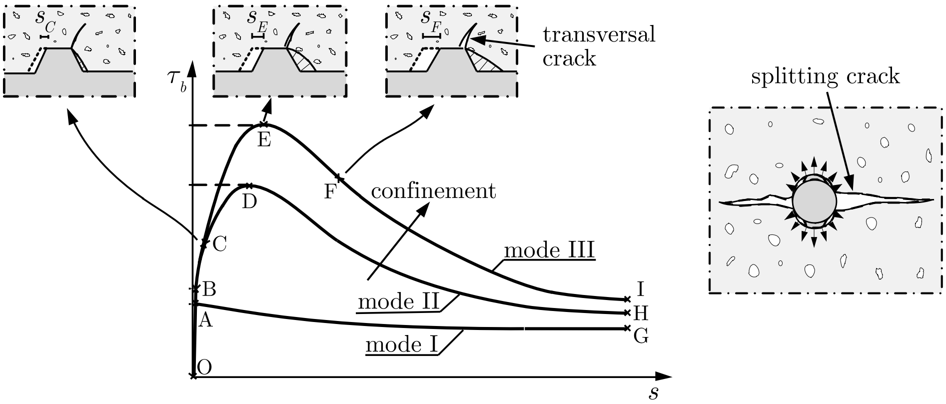

Figure 2: Typical response under monotonic loading, adapted from FIB [2].

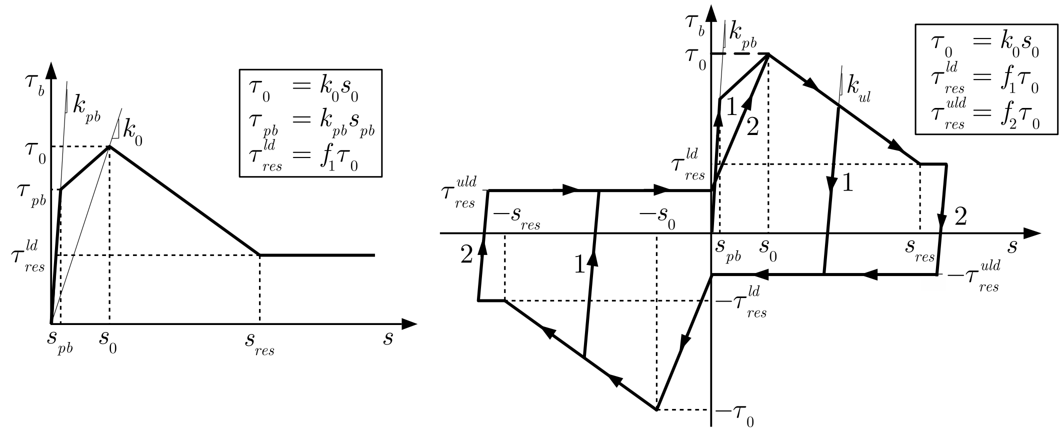

(a) monotonic loading (b) reversed cyclic loading

Figure 3: Schematic representation of the base model.

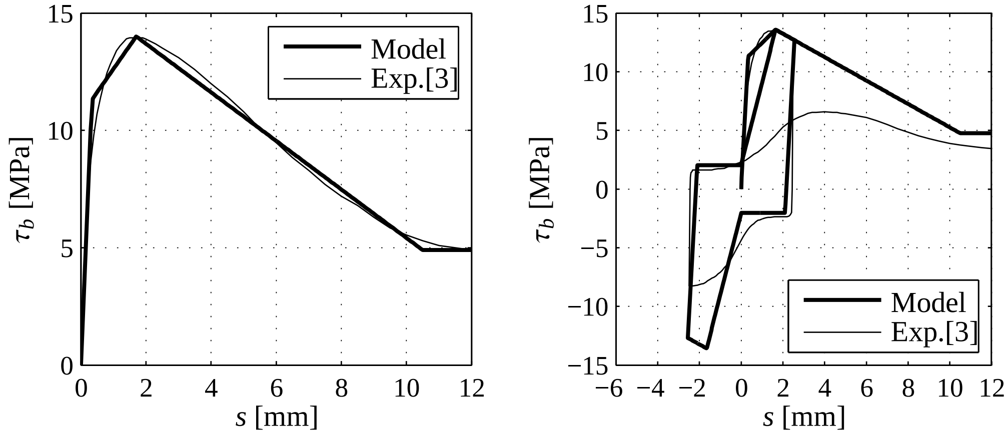

(a) monotonic loading (b) reversed cyclic loading

Model parameters: $k_{pb} = k_{ul} = 32.94$ GPa/m, $k_0 = 8.235$ GPa/m, $s_{pb} = 0.343$ mm, $s_0 = 1.70$ mm, $s_{res} = 10.50$ mm, $f_1 = 0.35$, $f_2 = 0.15$.

Figure 4: Base model - Comparison with experimental data.

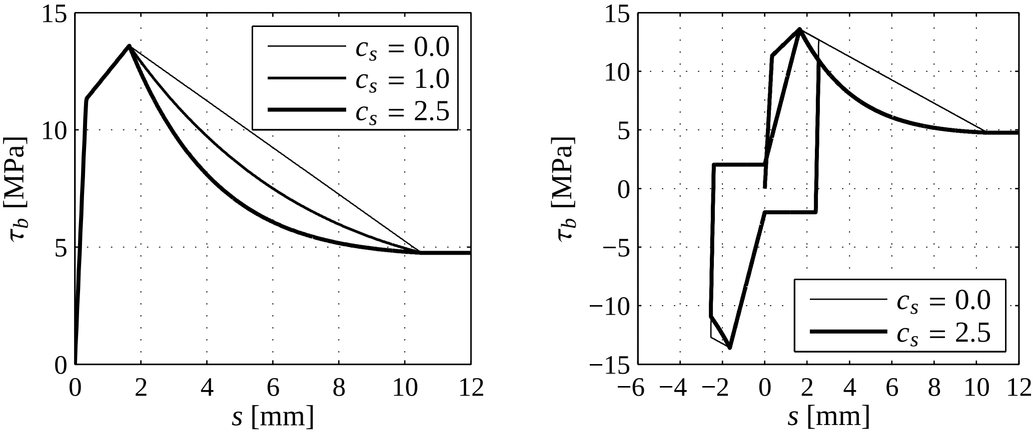

(a) monotonic loading

(b) reversed cyclic loading

Figure 5: Effect of the parameter c_s in the simulation.

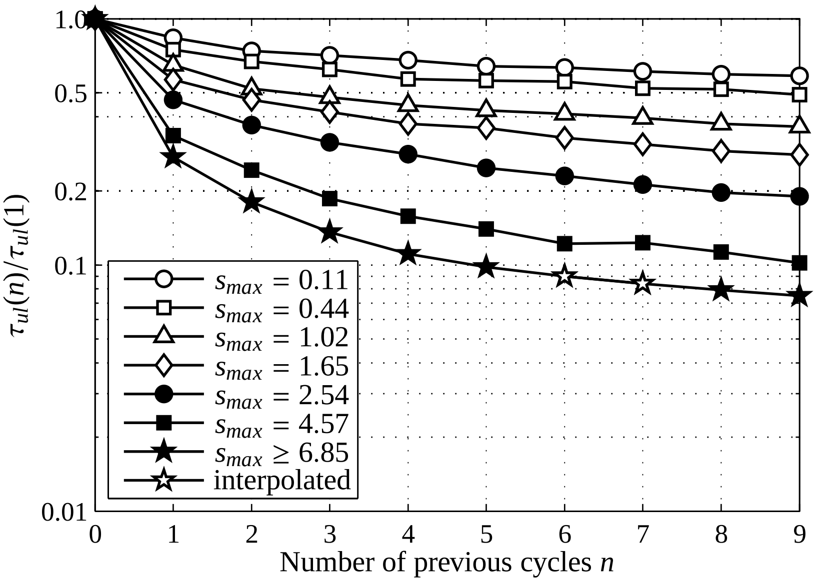

Figure 6: Bond strength deterioration with the number and amplitude of the cycles, adapted from Eligehausen *et al.* [3].

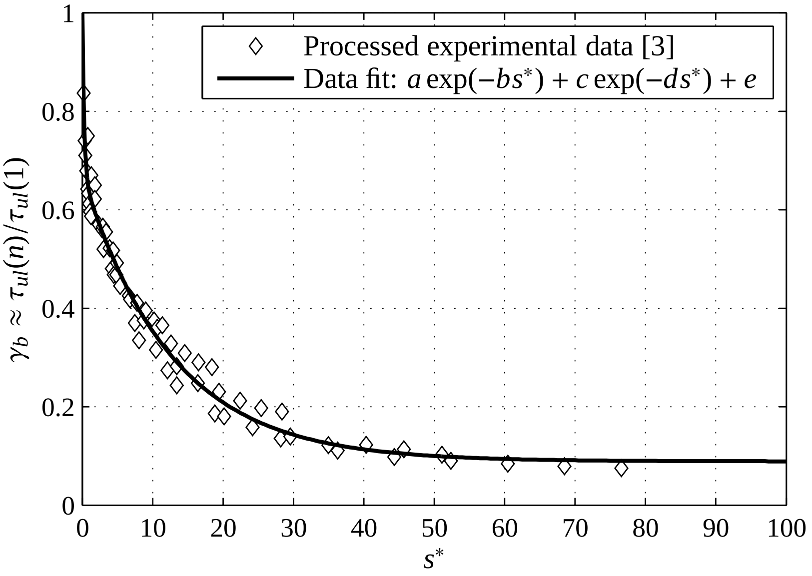

Figure 7: Relation between the cyclic peak stress ratio and the parameter s^*.

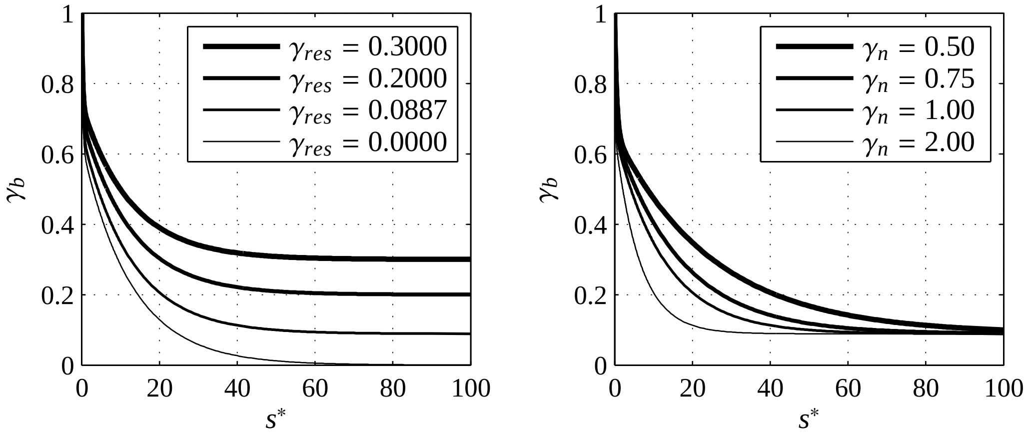

(a) effect of the parameter γ_{res} ($\gamma_n = 1.00$)　(b) effect of the parameter γ_n ($\gamma_{res} = 0.0887$)

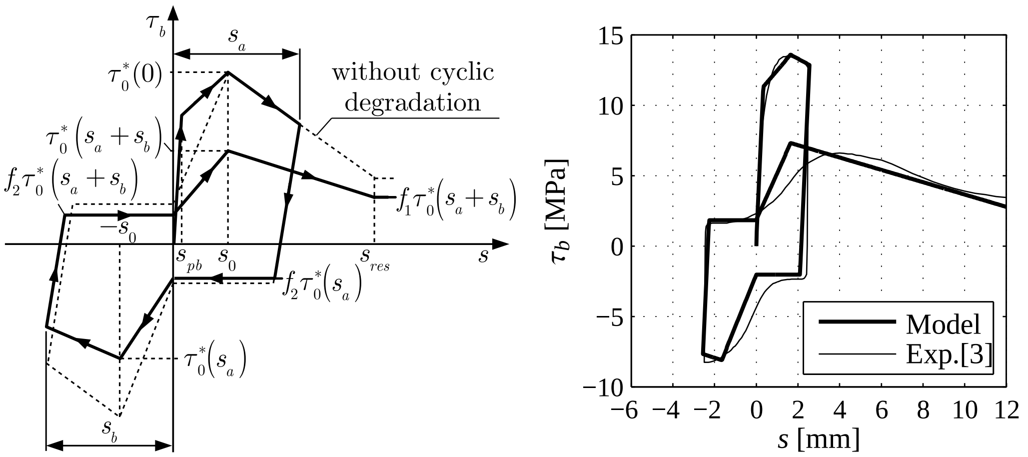

(c) schematic representation　(d) comparison with experimental data

Model parameters in (d) are the same of Figure 4 and $\gamma_{res} = 0.0887$, $\gamma_n = 1.00$.

Figure 8: Sub-model for the cyclic resistance degradation.

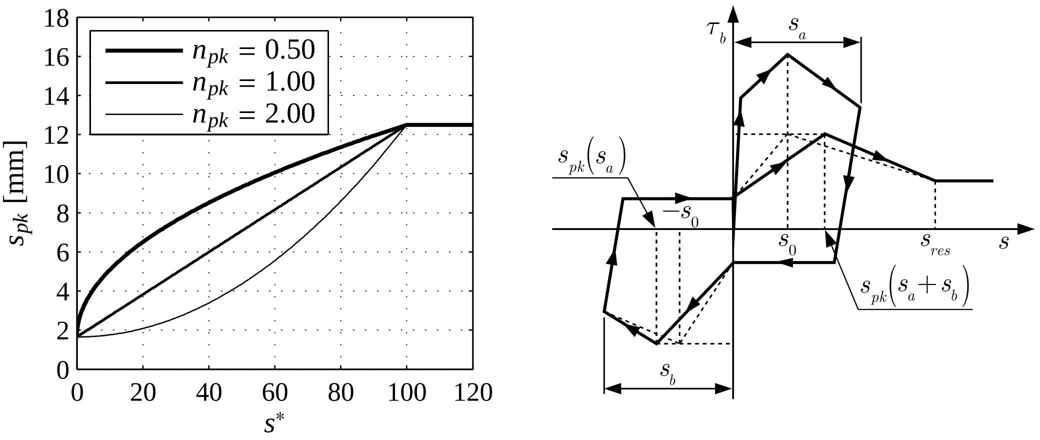

(a) effect of the parameter n_{pk}

(b) schematic representation

Model parameters in (a): s_0 = 1.65 mm, s_{res} = 12.5 mm.

Figure 9: Sub-model for the peak stress slip evolution.

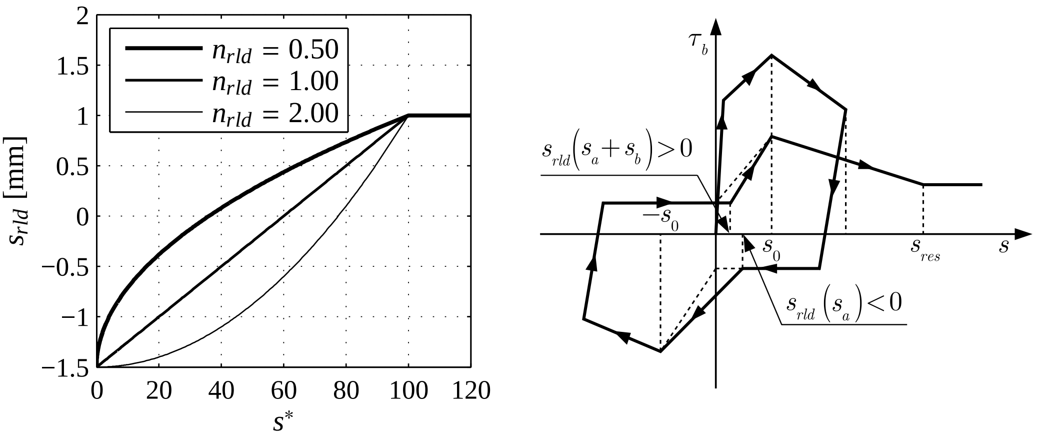

(a) effect of the parameter n_{rld}

(b) schematic representation

Model parameters in (a): $s_{rld}^0 = -1.5$ mm, $s_{rld}^\infty = +1.0$ mm.

Figure 10: Sub-model for the reload slip evolution.

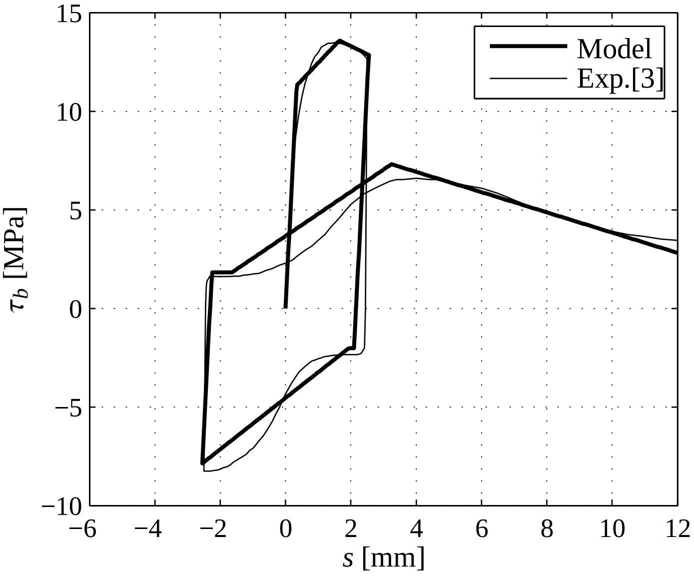

Model parameters are the same of Figure 8-d and $n_{pk} = 0.57$, $s^0_{rld} = -3.0$ mm, $s^\infty_{rld} = 9.0$ mm, $n_{rld} = 0.55$.

Figure 11: Comparison of the results obtained with the proposed bond model with experimental data.

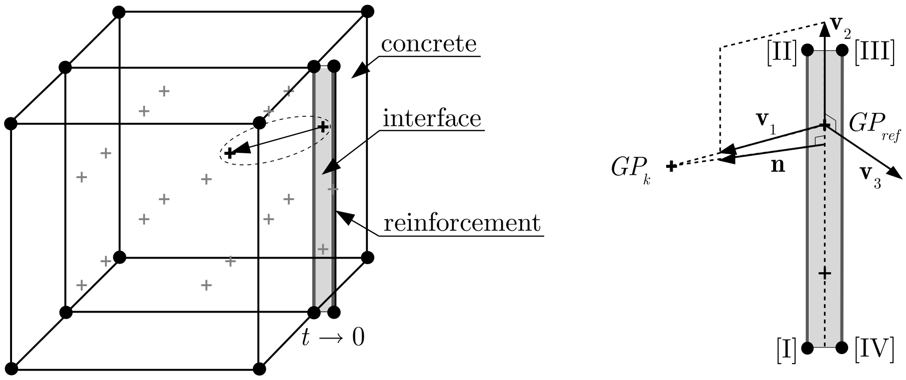

Figure 12: Radial stress effect - Computing the stress acting on the interface.

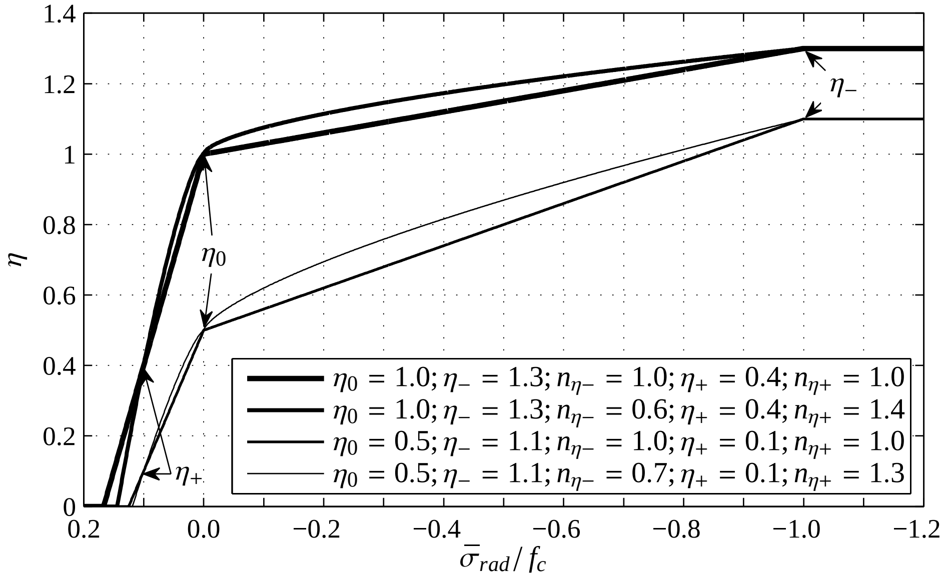

Figure 13: Radial stress effect: Influence of the parameters on the shape of the function η.

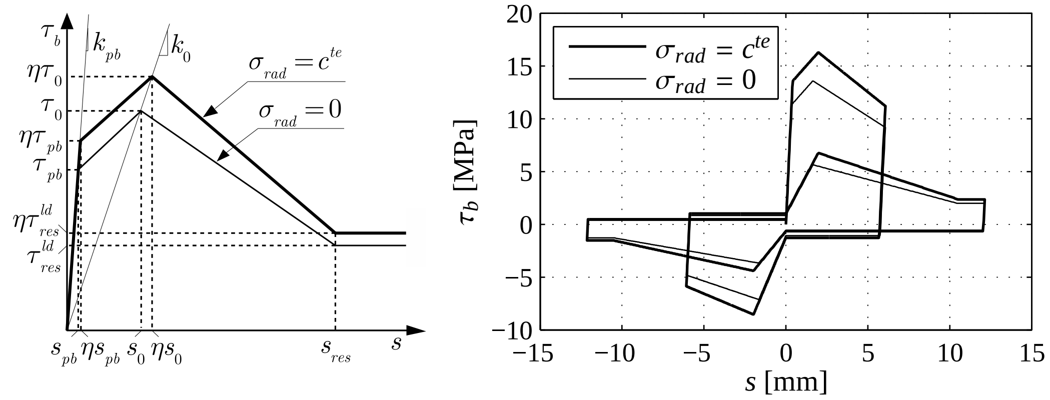

(a) schematic representation

(b) comparison with experimental data

Model parameters in (b) are the same of Figure 8 and $\sigma_{cf}/f_c = 0.50$, $\eta_0 = 1.00$, $\eta_- = 1.30$, $n_{\eta-} = 0.60$, $\eta_+ = 0.40$, $n_{\eta+} = 1.40$.

Figure 14: Radial stress effect for reversed cyclic loading.

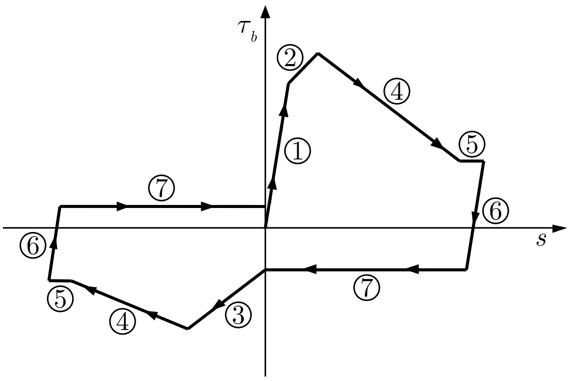

Figure 15: Bond model branch numbering.

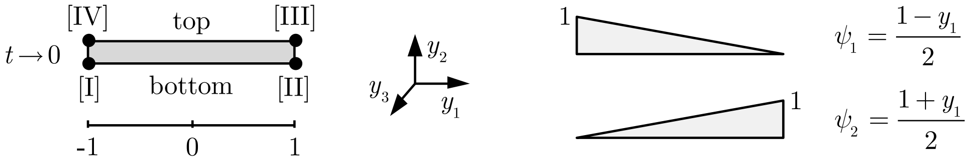

Figure 16: Zero thickness 4-noded isoparametric interface element.

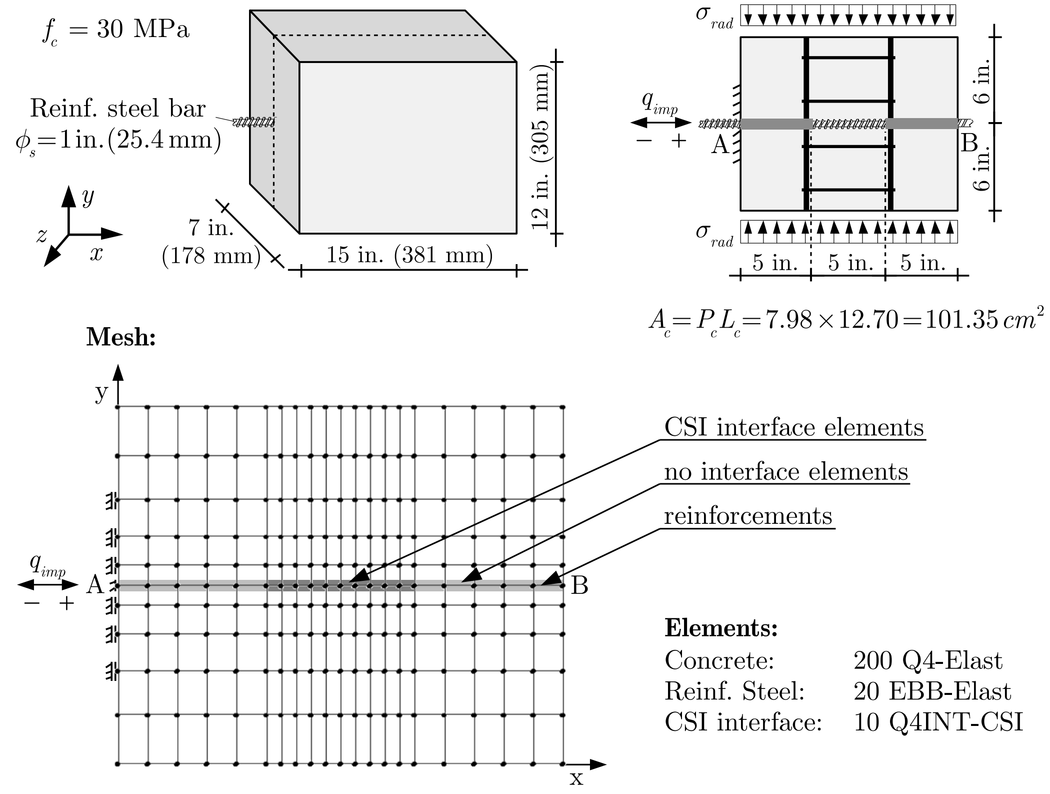

Figure 17: Example 1 - Geometric and mechanical characteristics and mesh used in the analyses.

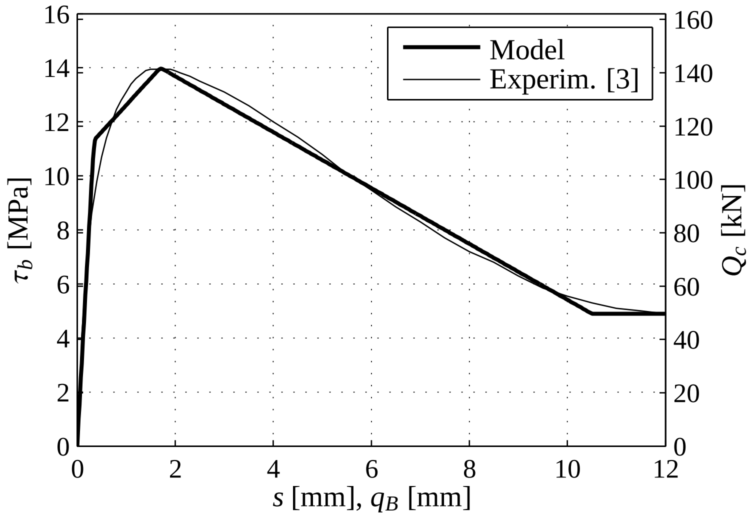

Figure 18: Example 1 (#1) - Response under monotonic loading

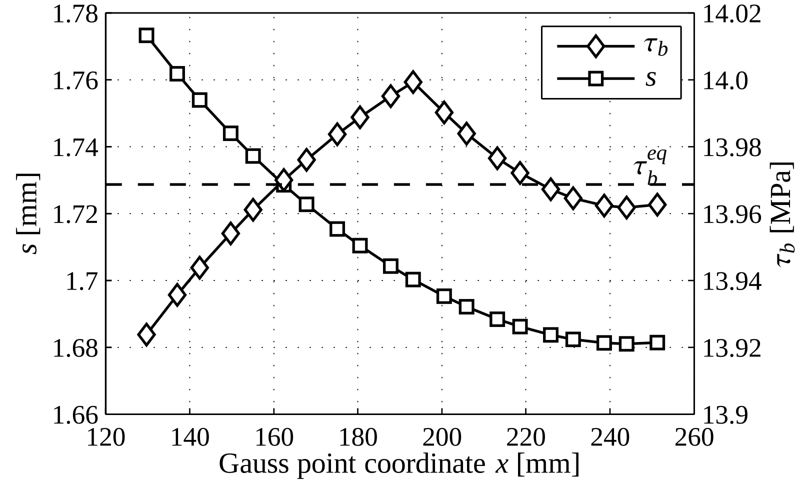

Figure 19: Example 1 (#1) - Bond stress and slip variation along the interface at peak force.

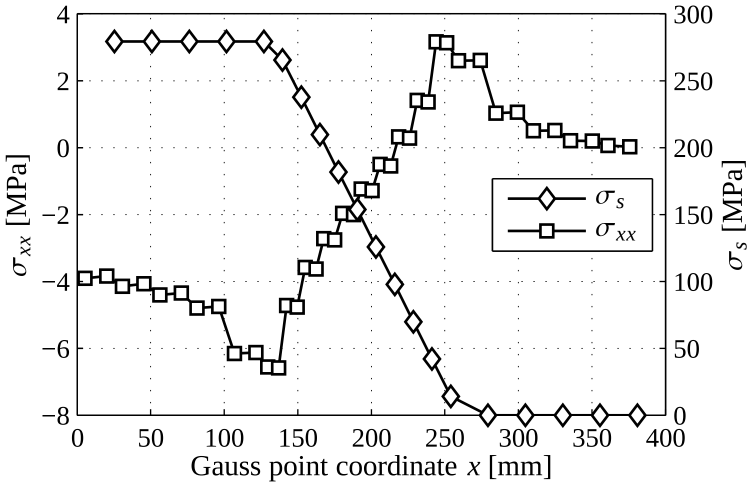

Figure 20: Example 1 (#1) - Steel axial stress and surrounding concrete stress at peak force.

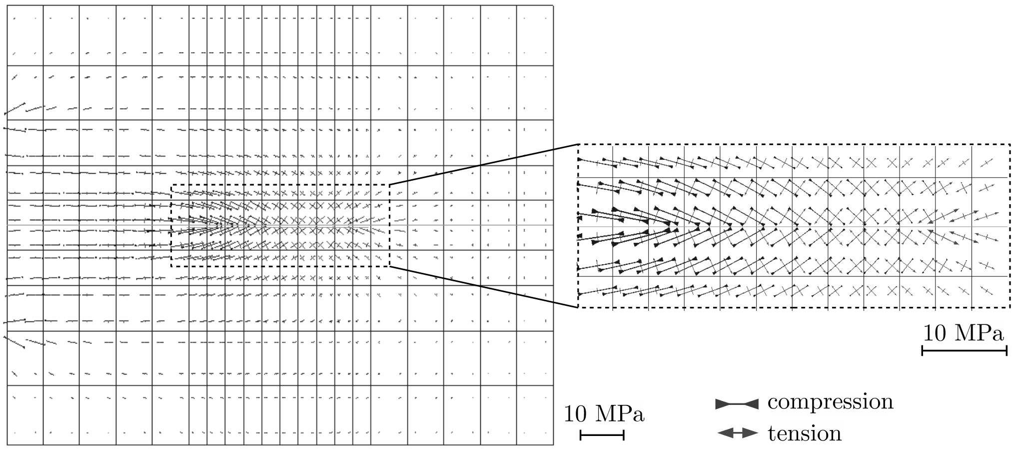

Figure 21: Example 1 (#1) - Principal stress vectors in the concrete elements at peak force.

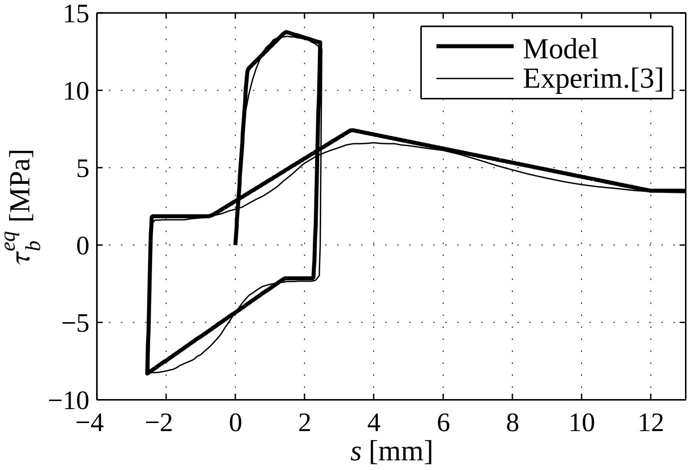

Figure 22: Example 1 (#2) - Equivalent bond stress *vs.* slip.

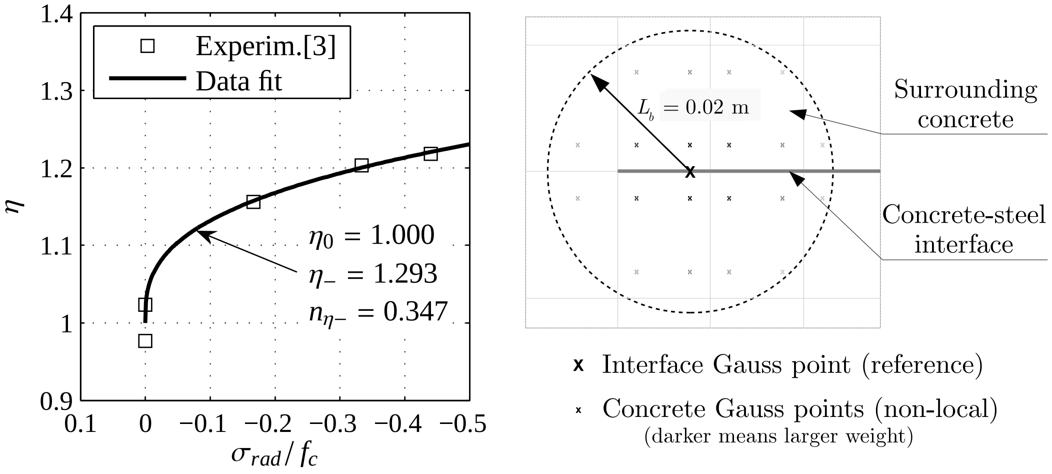

(a) calibration

(b) nonlocal radial stress computation

Figure 23: Example 1 (#3) - Radial stress sub-model.

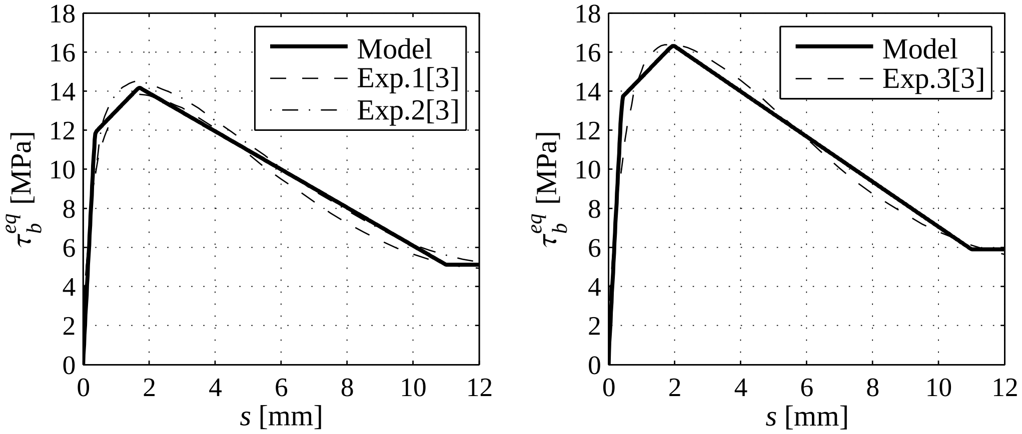

(a) σ_{rad} = 0.0 MPa (b) σ_{rad} = −5.0 MPa

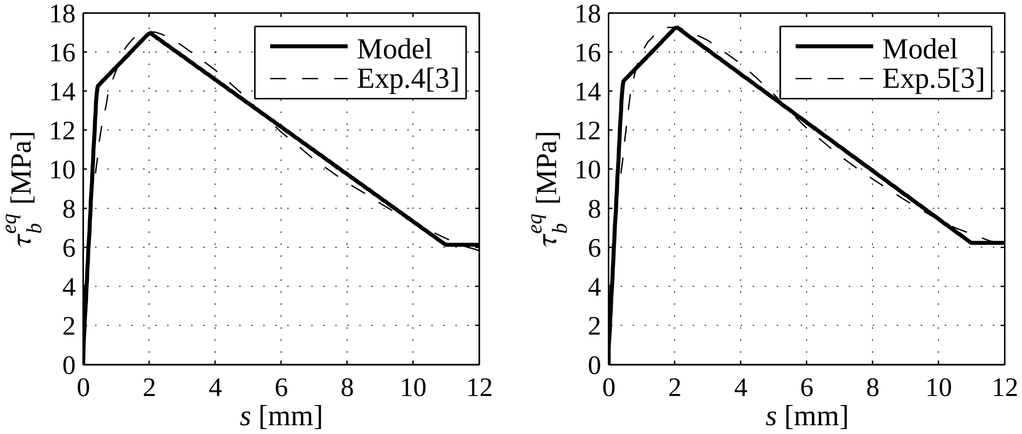

(c) σ_{rad} = −10.0 MPa (d) σ_{rad} = −13.2 MPa

Figure 24: Example 1 (#3) - The effect of the radial stress.

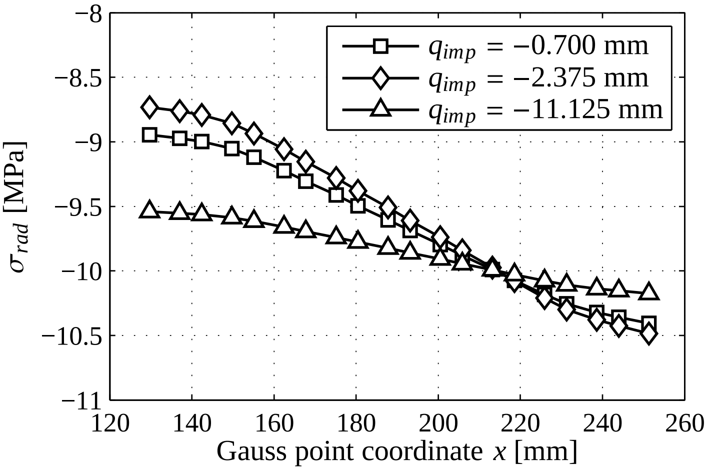

Figure 25: Example 1 (#3) - Computed nonlocal radial stresses along the anchorage ($\sigma_{rad} = -10.0$ MPa).

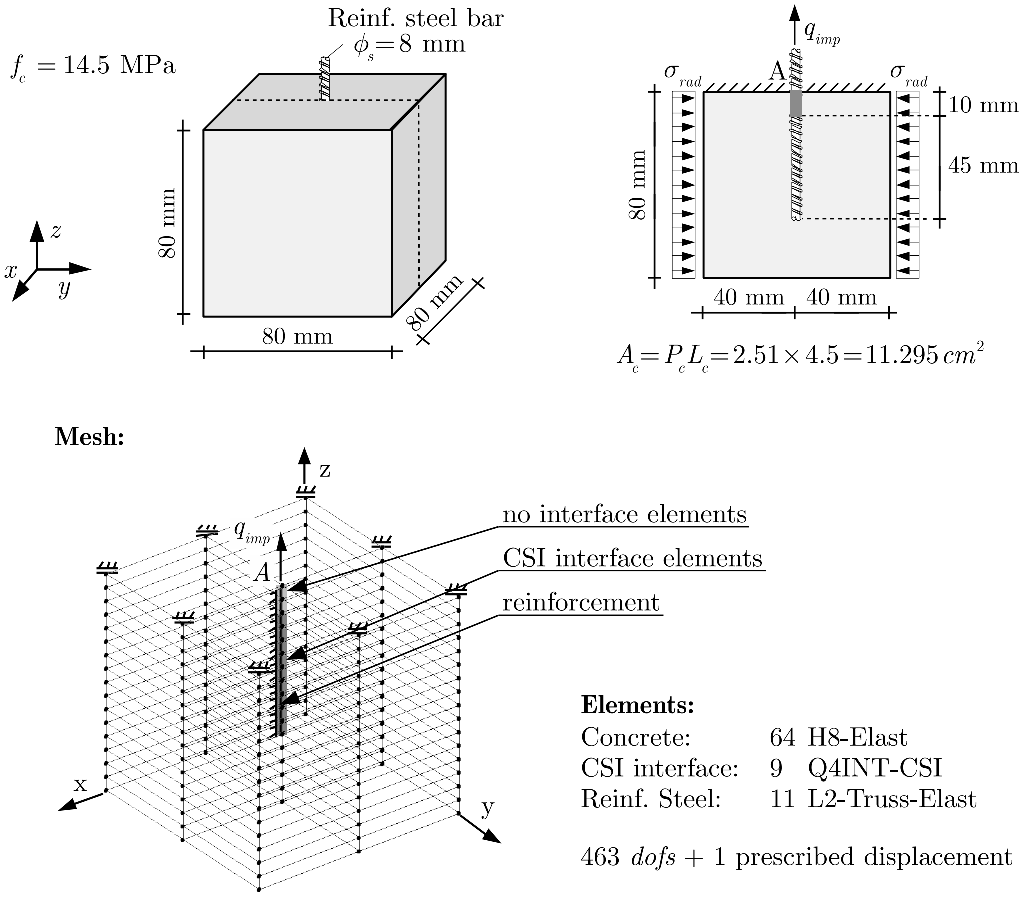

Figure 26: Example 2 - Geometric and mechanical characteristics and mesh used in the analyses.

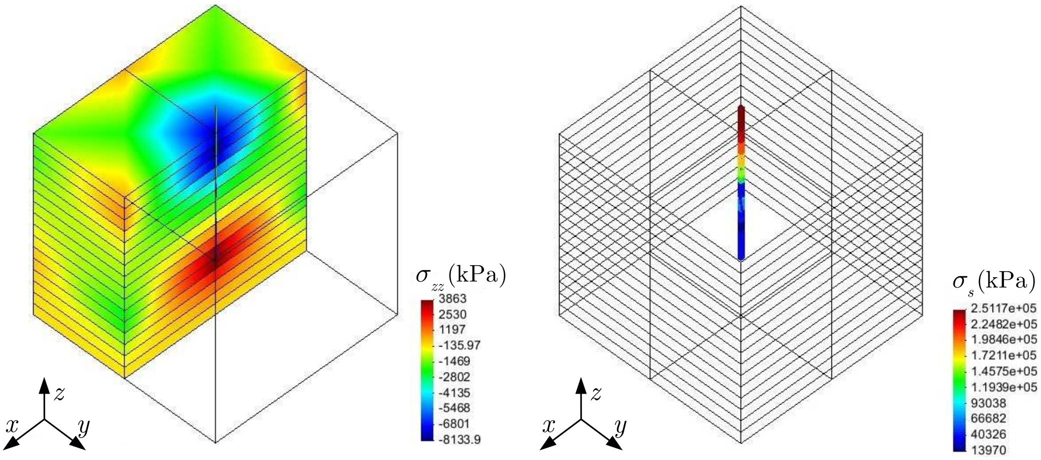

(a) σ_{zz} in the concrete elements

(b) axial stress distribution in the reinf. steel bar

Figure 27: Example 2 - Analysis without external radial stress (σ_{rad} = 0.0 MPa, q_{imp} = 1.20 mm).

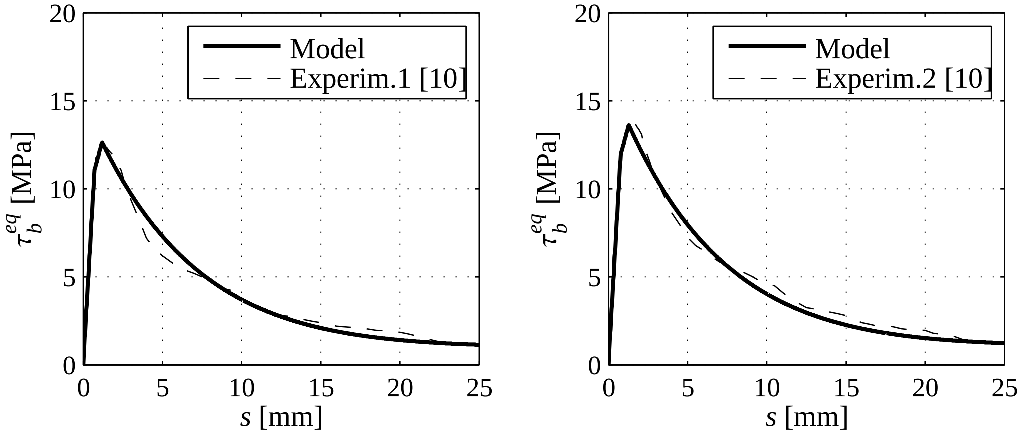

(a) $\sigma_{rad} = 0.0$ MPa

(b) $\sigma_{rad} = -5.0$ MPa

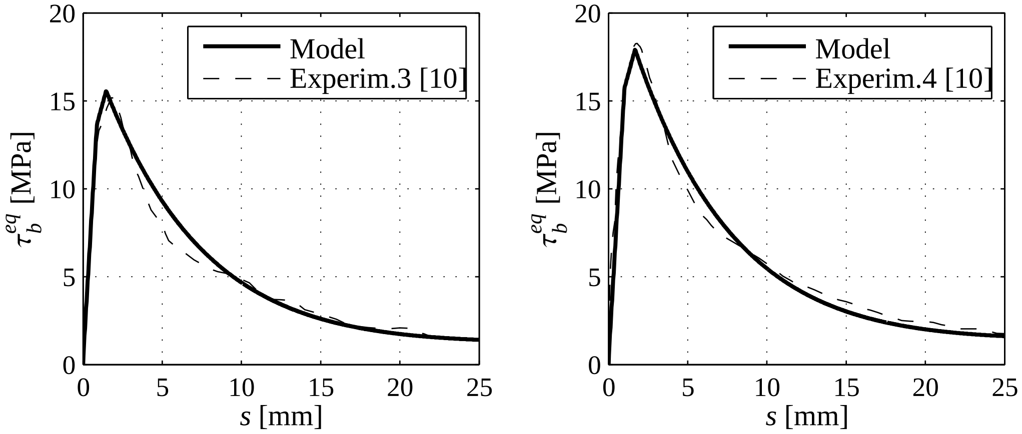

(c) $\sigma_{rad} = -10.0$ MPa

(d) $\sigma_{rad} = -15.0$ MPa

Figure 28: Example 2 - The effect of the radial stress on the monotonic response.

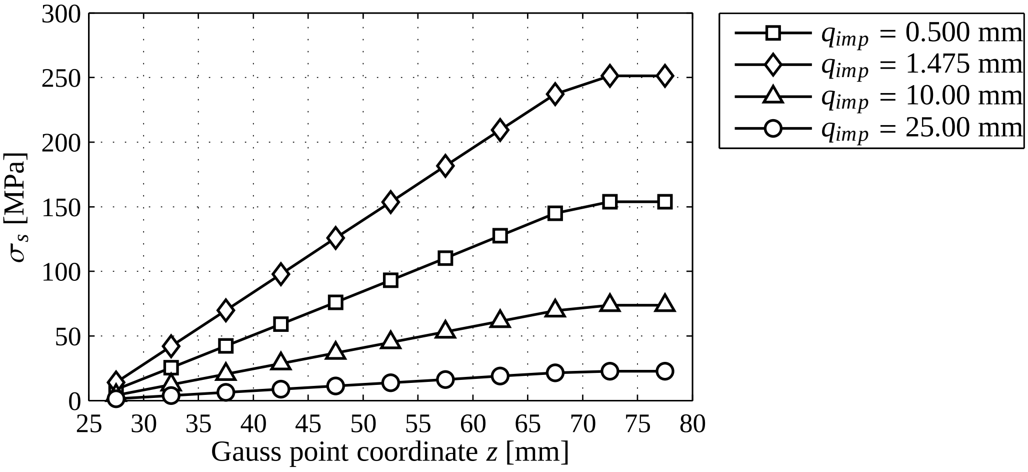

Figure 29: Axial stress distribution along the interface at chosen steps (σ_{rad} = 0.0 MPa).

List of Tables

1 Bond model parameters. 68
2 Example 1 - Model parameters. 69
3 Example 1 - Characteristics of the analyses 70
4 Example 2 - Model parameters. 71

Table 1: Bond model parameters.

Param.	Unit	Definition	Domain
k_{pb}	Pa/m	perfect bond tangent stiffness	$[0, \infty]$
k_0	Pa/m	monotonic secant stiffness at peak stress	$[0, \infty]$
k_{ul}	Pa/m	unloading stiffness	$[0, \infty]$
s_{pb}	m	monotonic perfect bond slip limit	$[0, s_0]$
s_0	m	monotonic slip at peak stress	$\left[s_{pb}, s_{res}\right]$
s_{res}	m	slip at the beginning of the loading residual stress	$[s_0, \infty]$
f_1	-	loading residual stress ratio	$[0, 1]$
f_2	-	unloading residual stress ratio	$[0, 1]$
c_s	-	controls the shape of the softening branch	$[0, \infty]$
γ_{res}	-	γ_b at $s^* = 100$	$[0, 1]$
γ_n	-	controls the evolution of γ_b	$[0, \infty]$
n_{pk}	-	controls the evolution of s_{pk}	$[0, \infty]$
s_{rld}^0	m	reload slip for $s^* = 0$	$\left[-s_{res}, s_{rld}^{\infty}\right]$
s_{rld}^{∞}	m	reload slip for $s^* = \infty$	$\left[-s_{rld}^0, s_{res}\right]$
n_{rld}	-	controls the evolution of s_{rld}	$[0, \infty]$
L_b	m	bond length	$[0, \infty]$
f_c	Pa	concrete resistance under compression	$[0, \infty]$
η_0	-	value of η for $\bar{\sigma}_{rad} = 0$	$[0, \infty]$
η_-	-	value of η for $\bar{\sigma}_{rad} = -f_c$	$[0, \infty]$
η_+	-	value of η for $\bar{\sigma}_{rad} = 0.10 f_c$	$[0, \infty]$
$n_{\eta-}$	-	controls the evolution of η for negative values of $\bar{\sigma}_{rad}$	$[0, \infty]$
$n_{\eta+}$	-	controls the evolution of η for positive values of $\bar{\sigma}_{rad}$	$[0, \infty]$

Table 2: Example 1 - Model parameters.

Model	**Type**	**Parameters**
#1	Elastic	$E = 30.5$ GPa, $\nu = 0.20$, $t = 0.178$m (plane stress)
#2	EBB	$E = 200.0$ GPa, $\nu = 0.30$, $A_s = 5.067$ cm^2, $I_z = 2.043$ cm^4
#3	CSI	$k_{pb} = 32.94$ GPa/m, $k_0 = 8.235$ GPa/m, $k_{ul} = 90.0$ GPa/m, $k_{o2} = k_{o3} = 1000$ GPa/m, $s_{pb} = 0.343$ mm, $s_0 = 1.70$ mm, $s_{res} = 10.50$ mm, $c_s = 0.0$, $f_1 = 0.35$, $f_2 = 0.00$, $\gamma_{res} = 1.0$, $\gamma_n = 1.0$, $n_{pk} = 1.00$, $s^0_{rld} = 0.00$ mm, $s^\infty_{rld} = 0.00$ mm, $n_{rld} = 1.00$, $l_\eta = 0.00$ m, $f_c = 0.0$ MPa, $\eta_0 = 1.0$, $\eta_- = 1.0$, $\eta_+ = 1.0$, $n_{\eta-} = 1.0$, $n_{\eta+} = 1.0$
#4	CSI	$k_{pb} = 9.50$ GPa/m, $k_0 = 8.235$ GPa/m, $k_{ul} = 90.0$ GPa/m, $k_{o2} = k_{o3} = 1000$ GPa/m, $s_{pb} = 0.343$ mm, $s_0 = 1.45$ mm, $s_{res} = 12.00$ mm, $c_s = 0.0$, $f_1 = 0.47$, $f_2 = 0.25$, $\gamma_{res} = 0.45$, $\gamma_n = 3.5$, $n_{pk} = 0.57$, $s^0_{rld} = -3.00$ mm, $s^\infty_{rld} = 9.00$ mm, $n_{rld} = 0.55$, $l_\eta = 0.00$ m, $f_c = 0.0$ MPa, $\eta_0 = 1.0$, $\eta_- = 1.0$, $\eta_+ = 1.0$, $n_{\eta-} = 1.0$, $n_{\eta+} = 1.0$
#5	CSI	$k_{pb} = 8.35$ GPa/m, $k_0 = 8.235$ GPa/m, $k_{ul} = 90.0$ GPa/m, $k_{o2} = k_{o3} = 1000$ GPa/m, $s_{pb} = 0.360$ mm, $s_0 = 1.70$ mm, $s_{res} = 11.00$ mm, $c_s = 0.0$, $f_1 = 0.36$, $f_2 = 0.00$, $\gamma_{res} = 1.0$, $\gamma_n = 1.0$, $n_{pk} = 1.00$, $s^0_{rld} = 0.00$ mm, $s^\infty_{rld} = 0.00$ mm, $n_{rld} = 1.00$, $l_\eta = 0.02$ m, $f_c = 30.0$ MPa, $\eta_0 = 1.0$, $\eta_- = 1.293$, $\eta_+ = 1.0$, $n_{\eta-} = 0.347$, $n_{\eta+} = 1.0$

Table 3: Example 1 - Characteristics of the analyses

Analysis	**Models** (see Table 2)	**Loads** (see Figure 17)
#1	Conc. #1, Reinf. #2, CSI #3	q_{imp} (monotonic), $\sigma_{rad} = 0.0$ MPa
#2	Conc. #1, Reinf. #2, CSI #4	$q_{imp} = \{0.0, 2.7, -2.7, 13.0\}$ mm, $\sigma_{rad} = 0.0$ MPa
#3	Conc. #1, Reinf. #2, CSI #5	q_{imp} (monotonic), $\sigma_{rad} = \{0.0, -5.0, -10.0, -13.2\}$ MPa

Table 4: Example 2 - Model parameters.

Model	**Type**	**Parameters**
#1	Elastic	E = 15.5 GPa, ν = 0.17
#2	Elastic	E = 200.0 GPa, ν = 0.30, A_s = 0.5026 cm^2
#3	CSI	k_{pb} = 14.40 GPa/m, k_0 = 9.72 GPa/m, k_{ul} = 90.0 GPa/m, $k_{o2} = k_{o3}$ = 1000 GPa/m, s_{pb} = 0.68 mm, s_0 = 1.15 mm, s_{res} = 25.00 mm, c_s = 2.8, f_1 = 0.09, f_2 = 0.00, γ_{res} = 1.0, γ_n = 1.0, n_{pk} = 1.00, s^0_{rld} = 0.00 mm, s^∞_{rld} = 0.00 mm, n_{rld} = 1.00, l_η = 15 cm, f_c = 14.5 MPa, η_0 = 1.0, $\eta_- = 1.418, \eta_+ = 1.0, n_{\eta-} = 1.562, n_{\eta+} = 1.0$